

**Investigating the Effects of two external  
Parameters on an idealized Convective  
Atmospheric Boundary Layer Entrainment Layer  
using Large Eddy Simulation**

by

Niamh Chaparro

A THESIS SUBMITTED IN PARTIAL FULFILLMENT  
OF THE REQUIREMENTS FOR THE DEGREE OF

**Master of Science (MSc)**

in

THE FACULTY OF GRADUATE AND POSTDOCTORAL  
STUDIES  
(Earth, Ocean and Atmospheric Sciences)

The University Of British Columbia  
(Vancouver)

December 2014

© Niamh Chaparro, 2014

# Table of Contents

<b>Table of Contents . . . . .</b>	<b>ii</b>
<b>List of Tables . . . . .</b>	<b>vi</b>
<b>List of Figures . . . . .</b>	<b>vii</b>
<b>Glossary . . . . .</b>	<b>ix</b>
<b>1 Introduction . . . . .</b>	<b>1</b>
1.1 Motivation . . . . .	1
1.2 Relevant Background . . . . .	2
1.2.1 The Convective Boundary Layer (CBL) . . . . .	2
1.2.2 CBL Height ( $h$ ) . . . . .	6
1.2.3 CBL Growth by Entrainment . . . . .	7
1.2.4 The CBL Entrainment Layer (EZ) . . . . .	7
1.2.5 Modelling the CBL and EZ . . . . .	9
1.2.6 Scales and Scaling Relations of the CBL and EZ . . . . .	13
1.3 Research Questions . . . . .	19
1.4 Approach to Research Questions . . . . .	21
<b>2 Tools . . . . .</b>	<b>25</b>
2.1 Large Eddy Simulation . . . . .	25
2.2 Handling of Output . . . . .	26
2.2.1 Tri-Linear Fit for Determining local ML height $h_0^l$ . .	27

<b>3</b>	<b>Output Verification . . . . .</b>	<b>29</b>
3.1	Initialization and Spin-Up Time . . . . .	29
3.2	Horizontally and ensemble averaged Potential Temperature $\bar{\theta}$ and Heat Flux $\overline{w'\theta'}$ Profiles . . . . .	33
3.3	FFT Energy Spectra . . . . .	35
3.4	Visualization of Structures within the Entrainment Zone . . .	36
3.5	Summary of Findings . . . . .	36
<b>4</b>	<b>Research Answers . . . . .</b>	<b>38</b>
4.1	Q1 Entrainment Zone Structure . . . . .	40
4.1.1	Local Mixed Layer Heights ( $h_0^l$ ) . . . . .	40
4.1.2	Local turbulent Velocity and Potential Temperature Fluctuations . . . . .	43
4.1.3	Downward Moving Warm Air at $h$ . . . . .	46
4.1.4	Answer to Q1 Entrainment Zone Structure . . . . .	48
4.2	Q2 Entrainment Zone Boundaries . . . . .	50
4.2.1	EZ Boundaries based on the average vertical Potential Temperature Gradient Profiles . . . . .	50
4.2.2	EZ Boundaries based on scaled vertical Potential Temperature Gradient Profiles . . . . .	55
4.2.3	EZ Boundaries based on scaled Heat Flux Profiles . .	57
4.2.4	Answer to Q2 Entrainment Zone Boundaries . . . . .	59
4.3	Q3 Entrainment Rate Parameterization . . . . .	60
4.3.1	Reminder of Definitions . . . . .	60
4.3.2	CBL Growth . . . . .	60
4.3.3	Heights based on the scaled vertical average Potential Temperature Profile . . . . .	64
4.3.4	Heights based on the scaled vertical average Heat Flux Profile . . . . .	66
4.3.5	Answer to Q3 Entrainment Rate Parameterization . .	66
<b>5</b>	<b>Results in Context . . . . .</b>	<b>68</b>
5.1	Comparison of general Set-up . . . . .	70

5.1.1	Significance of Grid-size . . . . .	70
5.1.2	Horizontal Domain . . . . .	71
5.1.3	Initial Conditions . . . . .	72
5.2	Entrainment Zone Structure . . . . .	72
5.2.1	Local ML Heights . . . . .	72
5.2.2	Local ML Height Distributions . . . . .	73
5.2.3	Local vertical Velocity and Potential Temperature Fluctuations . . . . .	74
5.2.4	Downward moving warm Air at $h$ . . . . .	74
5.3	Entrainment Zone Boundaries . . . . .	76
5.3.1	Direct Comparison based on the vertical Heat Flux Profile . . . . .	76
5.3.2	General Comparison using the Potential Temperature Profile . . . . .	78
5.4	Entrainment Rate Parameterization . . . . .	80
5.4.1	Direct Comparison based on the vertical Heat Flux Profile . . . . .	80
5.4.2	Extending Comparison to the average Potential Temperature Profile . . . . .	81
<b>6</b>	<b>Conclusion . . . . .</b>	<b>82</b>
6.1	Major Findings . . . . .	82
6.1.1	The gradient Method for determining local Heights based on the $\theta$ Profile is problematic. . . . .	82
6.1.2	CBL Height and EZ Boundaries can be defined based on the average Potential Temperature Profile . . . . .	83
6.1.3	Upper Lapse-Rate is a critical Parameter in idealized CBL Entrainment . . . . .	83
6.1.4	There are two CBL Entrainment Regimes . . . . .	84
6.2	Future Work . . . . .	84
6.2.1	Expand local CBL height determination Method . . .	84
6.2.2	Examine Resolution Effects . . . . .	84
6.2.3	Further explore Entrainment Regimes . . . . .	85

6.2.4	Apply a Mass Flux Scheme . . . . .	85
<b>References</b>	. . . . .	<b>86</b>
<b>7 Appendices</b>	. . . . .	<b>90</b>
7.1	Potential Temperature: $\theta$ . . . . .	90
7.2	Second Law of Thermodynamics . . . . .	91
7.3	Reynolds Decomposition and Simplification of Conservation of Enthalpy (or Entropy) for a dry Atmosphere . . . . .	91
7.4	Reynolds averaged Turbulence Kinetic Energy Equation . . .	92

# List of Tables

Table 1.1	Height definitions . . . . .	23
Table 3.1	Runs in terms of $\overline{w'\theta'_s}$ and initial lapse rate $\gamma$ . . . . .	30
Table 4.1	Height definitions . . . . .	61
Table 5.3	EZ Definitions used in comparable Studies . . . . .	78

# List of Figures

Figure 1.1	Lidar backscatter image of the CBL . . . . .	3
Figure 1.2	Visualization of entrainment from an LES . . . . .	4
Figure 1.3	Idealized vertical average profiles for a dry CBL . . . . .	5
Figure 1.4	Zero order CBL . . . . .	10
Figure 1.5	Alternative Potential Temperature Scale for the EZ . . . . .	15
Figure 1.6	Height definitions . . . . .	24
Figure 3.1	Scaled time vs Time . . . . .	31
Figure 3.2	Profiles of $\bar{\theta}$ , $\frac{\partial \bar{\theta}}{\partial z}$ and $\overline{w' \theta'}$ . . . . .	32
Figure 3.3	$\overline{w' \theta'}$ scaled by $(\overline{w' \theta'})_s$ . . . . .	32
Figure 3.4	$\bar{\theta}$ profiles at 2 hours for all runs . . . . .	33
Figure 3.5	Scaled $(\overline{w' \theta'})_s$ profiles at 3 hours for all runs . . . . .	34
Figure 3.6	FFT energy spectra of turbulent Velocity . . . . .	35
Figure 3.7	2D horizontal slices of $\theta'$ and $w'$ . . . . .	37
Figure 4.1	High local ML . . . . .	41
Figure 4.2	Low local ML . . . . .	41
Figure 4.3	Local ML height distributions . . . . .	42
Figure 4.4	Two-dimensional distributions of $w'$ and $\theta'$ for all runs . .	44
Figure 4.5	Two-dimensional distributions of $\frac{w'}{w^*}$ and $\frac{\theta'}{\theta^*}$ for all runs .	45
Figure 4.6	Downward moving warm air at $h$ . . . . .	46
Figure 4.7	Downward turbulent velocity perturbation at $h$ . . . . .	47
Figure 4.8	Positive potential temperature perturbation at $h$ (i) . . . .	48
Figure 4.9	Positive potential temperature perturbation at $h$ (ii) . . . .	49

Figure 4.10 Plot of scaled EZ upper ( $\frac{h_1}{h}$ ) and lower ( $\frac{h_0}{h}$ ) boundaries based on the average vertical potential temperature gradient profile. . . . .	50
Figure 4.11 $\frac{\partial \bar{\theta}}{\partial z}$ profiles with threshold at $.0002Kkm^{-1}$ . . . . .	51
Figure 4.12 Scaled EZ depth ( $\frac{h_1-h_0}{h}$ ) vs inverse Richardson number ( $Ri^{-1}$ ) with threshold at $.0002Kkm^{-1}$ . . . . .	52
Figure 4.13 Scaled EZ depth vs inverse Richardson Number with threshold at $.0004Kkm^{-1}$ . . . . .	53
Figure 4.14 Scaled EZ depth vs inverse Richardson number ( $Ri^{-1}$ ) with threshold at $.0001Kkm^{-1}$ . . . . .	54
Figure 4.15 Scaled $\frac{\partial \bar{\theta}}{\partial z}$ profiles with threshold at $.03$ . . . . .	55
Figure 4.16 scaled EZ depth vs $Ri^{-1}$ . . . . .	56
Figure 4.17 Log-log plot of scaled EZ depth vs $Ri^{-1}$ . . . . .	56
Figure 4.18 Scaled EZ Boundaries based on the vertical heat flux profile	57
Figure 4.19 scaled EZ depth vs $Ri^{-1}$ based on the vertical heat flux profile . . . . .	58
Figure 4.20 Height definitions . . . . .	60
Figure 4.21 $h$ vs time for all runs . . . . .	62
Figure 4.22 $h$ vs time for all runs on log-log coordinates . . . . .	62
Figure 4.23 $\frac{z_f}{h}$ vs Time . . . . .	63
Figure 4.24 Richardson numbers based on $\frac{\partial \bar{\theta}}{\partial z}$ . . . . .	64
Figure 4.25 Scaled entrainment rate vs inverse Richardson number . .	65
Figure 4.26 Richardson numbers based on $\frac{\bar{w}'\theta'}{\bar{w}'\theta'_s}$ . . . . .	66
Figure 4.27 Scaled entrainment rate vs inverse Richardson number (ii) .	67
Figure 5.1 Illustration of EZ Potential Temperature Scale based on $\gamma$	75
Figure 5.2 Plot of the relationship between scaled EZ depth and Richardson number from Federovich et al.'s (2004) . . . . .	77
Figure 5.3 Relationship of Scaled EZ depth to Richardson number from Brooks and Fowler's (2012) . . . . .	79
Figure 5.4 Plots of scaled entrainment rate vs Richardson number from Garcia and Mellado (2014) . . . . .	81

# Glossary

**CBL** Convective Boundary Layer

**DNS** Direct Numerical Simulation

**EL** Entrainment Layer

**EZ** Entrainment Zone

**FA** Free Atmosphere

**FFT** Fast Fourier Transform

**GCM** General Circulation Model

**ML** Mixed Layer

**LES** Large Eddy Simulation

**Ri** Richardson Number, the bulk Richardson Number is  $\frac{gh}{\theta_{ML}} \frac{\Delta\theta}{w^{*2}}$ ,  $\Delta\theta = \bar{\theta}(h_1) - \bar{\theta}(h_0)$

**TKE** Turbulence Kinetic Energy

# 1. Introduction

## 1.1 Motivation

The daytime convective atmospheric boundary layer (CBL) over land starts to grow after sunrise when the surface becomes warmer than the air above it. Coherent turbulent structures (thermals) begin to form and rise, since their relative warmth causes them to be less dense than their surroundings, and so buoyant. The temperature profile of the residual boundary layer is stable; i.e., potential temperature ( $\theta$ , see Section 7.1) increases with height. The thermals rise to their neutral buoyancy level, overshoot, and then overturn or recoil. Concurrently, warm stable air from the free atmosphere (FA) above is trapped or enveloped and subsequently mixed into the growing turbulent mixed layer (ML) (Stull 1988). This mixing at the top of the CBL is known as entrainment and the region over which it occurs, the entrainment zone (EZ, Deardorff et al. 1980). A common, simplified conceptual model of this case is the dry shear free CBL (Sullivan et al. 1998, Federovich et al. 2004 Brooks and Fowler 2012). This model serves as an intellectually accessible way to understand the dynamic and complex CBL and its EZ.

CBL height ( $h$ ) and the prediction thereof are important for calculating the concentration of any atmospheric species within the ML as well as the sizes of the turbulent structures. In combination with the level at which clouds condense (lifting condensation level) knowledge of EZ depth facilitates predictions pertaining to the formation of cumulus clouds. For example cloud cover increases as more thermals rise above their lifting condensation level

(Wilde et al. 1985). Parameterizations for both CBL growth and EZ depth are required in mesoscale and general circulation models (GCMs). Furthermore it is an attractive goal to develop a robust set of scales for this region analogous to Monin-Obukov Theory (Stull 1988, Traumner et al. 2011, Steyn et al. 1999, Nelson et al. 1989, Sorbjan 1996).

Atmospheric CBL entrainment has been studied as a separate phenomenon (Nelson et al. 1989, Sullivan et al. 1998, Federovich et al. 2004, Brooks and Fowler 2012) as well as within the wider topic of entrainment in geophysical flows (Turner 1986). There is broad agreement as to the fundamental scaling parameters and relationships involved. However, the discussion as to how the parameters are defined and measured (Brooks and Fowler 2012, Traumner et al. 2011) and the exact forms of the resulting relationships continues (Sullivan et al. 1998, Federovich et al. 2004 Brooks and Fowler 2012). This prompts me to ask the research questions I build up to in Section 1.2 and outline in Section 1.3.

## 1.2 Relevant Background

### 1.2.1 The Convective Boundary Layer (CBL)

The CBL grows in three stages: (i) slowly after sunrise as the nighttime boundary layer is burned off, (ii) rapidly in the late morning as the top rises through the residual layer and again (iii) slowly, when the previous day's capping inversion is reached (Nelson et al. 1989). Convective turbulence and the dominant upward vertical motions then begin to subside as the surface cools. While the surface is warm, buoyancy driven thermals of somewhat uniform potential temperature ( $\theta$ ) and tracer concentration at their cores form and entrain surrounding air laterally as they rise, as well as trapping and mixing in stable warm from above (Stull 1988, Crum et al. 1987). Under conditions of strong convection and weak winds, buoyantly driven turbulence dominates and shear-driven turbulence is insignificant (Fedorovich and Conzemius 2001). Thermal overshoot relative to their neutral buoyancy

level, and subsequent entrainment of the warmer air from aloft augments the warming caused by the surface turbulent heat flux  $(\overline{w'\theta'})_s$  (see Section 7.1) and results in a  $\theta$  jump or inversion at the CBL top (Schmidt and Schumann 1989, Turner 1986). There may also be a residual inversion from the day before, possibly strengthened by subsidence (Stull 1988, Sullivan et al. 1998).

Lidar images such as Figure 1.1 show the overall structure of the CBL with rising thermals, impinging on the air above (Crum et al. 1987, Crum and Stull 1987, Traumner et al. 2011).

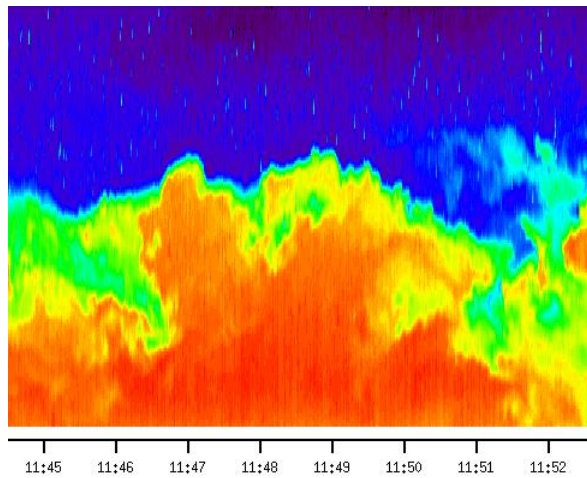


**Figure 1.1:** Lidar backscatter image of the CBL (property of Shane D. Mayor, Department of Geological and Environmental Sciences, California State University). Time is on the bottom axis, back-scatter intensity is represented by the colours red-blue. Red corresponds to high intensity, and therefore aerosol concentration. Regions with negligibly low concentrations are dark blue.

This has been effectively modelled using large eddy simulation (LES) by Schmidt and Schumann (1989) who used horizontal slices of turbulent potential temperature and vertical velocity fluctuations ( $\theta'$ ,  $w'$ ) at various vertical levels to show how the thermals form, merge and impinge at the CBL top with concurrent peripheral downward motions. The latter is supported

in the LES visualizations of Sullivan et al. (1998). The vertical cross section within the EZ in Figure 1.2 shows the relatively cooler thermals and trapped warmer air as well as the closely associated upward motion of cooler air and downward motion of warmer air.

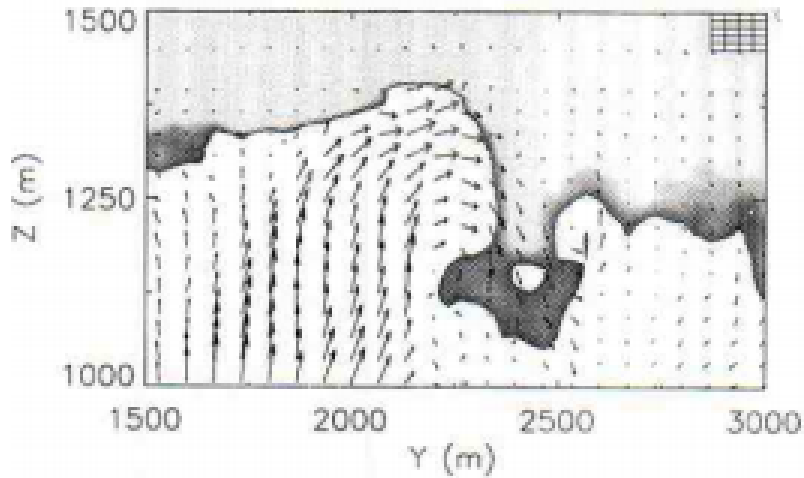


**Figure 1.2:** Flow visualization from Sullivan et al. 1998 showing a modelled CBL thermal enveloping FA air.

On average these convective turbulent structures create a fully turbulent mixed layer (ML) with eddy sizes cascading through an inertial subrange to the molecular scales at which energy is lost via viscous dissipation (Stull 1988). Here, as represented in Figure 1.3,  $\bar{\theta}$  is close to uniform and increases with respect to time due to  $(\overline{w'\theta'})_s$  and the downward flux of entrained stable air at the inversion  $(\overline{w'\theta'})_h$ . ML turbulence near the ground is dominated by warm updraughts and cool downdraughts. With proximity to the ML top, the updraughts become relatively cool and warmer FA air from above is drawn downward, so in the ML  $\overline{w'\theta'}$  is positive and decreasing. Directly above the ML the air is stable with intermittent turbulence and, on average, transitions from a uniform ML potential temperature ( $\frac{\partial \bar{\theta}}{\partial z} \approx 0$ ) to a stable lapse rate ( $\gamma$ ).

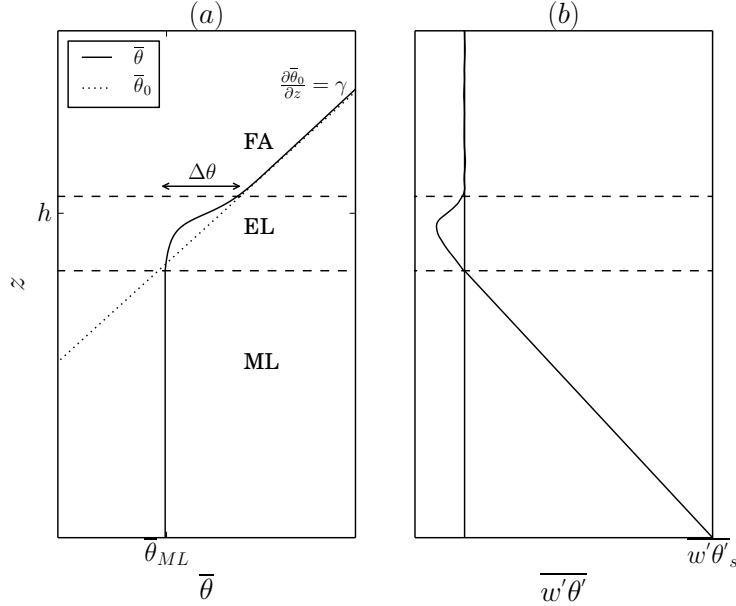


**Figure 1.3:** Idealized vertical average profiles for a dry CBL in the absence of large scale winds or subsidence. (a)  $\bar{\theta}_{ML}$  is the average mixed layer potential temperature.  $h$  is the height of maximum gradient in the  $\bar{\theta}$  profile. The initial  $\bar{\theta}$  profile which has a slope  $\gamma$  is represented by  $\bar{\theta}_0$  (dotted line). The mixed layer, entrainment zone and free atmosphere are denoted ML, EZ and FA respectively. (b)  $(w'\theta')_s$  is the average surface turbulent heat flux. The EZ boundaries (dashed lines) enclose the region of negative  $w'\theta'$ .

Nelson et al. (1989) outline the stages of CBL growth from when the sub-layers of the nocturnal boundary layer are entrained, until the previous day's capping inversion is reached and a quasi-steady growth is attained. The EZ depth relative to CBL height varies throughout these stages and its relationship to scaled entrainment exhibits hysteresis. Numerical studies typically represent this last quasi-steady phase involving a constant  $(\overline{w'\theta'})_s$  working against an inversion and/or a stable  $\gamma$  (Schmidt and Schumann 1989, Sorbjan 1996, Sullivan et al. 1998, Federovich et al. 2004, Brooks and Fowler 2012, Garcia and Mellado 2014).

### 1.2.2 CBL Height ( $h$ )

The ML is fully turbulent with a uniform average potential temperature ( $\bar{\theta}$ ) which increases sharply over the EZ. Aerosol and water-vapour concentrations decrease dramatically with transition to the stable upper FA. So any of these characteristics can support a definition of CBL height ( $h$ ). Nelson et al. (1989) defined  $h$  in terms of the percentage of ML air and identified it by eye from Lidar back-scatter images. Traumner et al. (2011) compared four automated methods applied to Lidar images:

- a suitable threshold value above which the air is categorized as ML air,
- the point of minimum (largest negative) vertical gradient,
- the point of minimum vertical gradient based on a fitted idealized curve,
- and the maximum wavelet covariance.

CBL height detection is a wide and varied field. Both Brooks and Fowler (2012) and Traumner et al. 2011 provide more thorough reviews.

Numerical models produce hundreds of local horizontal points from which smooth averaged vertical profiles are obtained, and statistically robust relationships inferred. Brooks and Fowler (2012) applied a wavelet technique to identify the height of maximum covariance in local vertical tracer profiles in their LES study. They compared this method to the gradient method i.e. locating the height of most negative vertical tracer concentration gradient, as well as the height of minimum  $\overline{w'\theta'}$  as shown later in Figure 1.6. This last definition is common among LES and laboratory studies where it has been referred to as the inversion height (Deardorff et al. 1980, Sorbjan 1996, Federovich et al. 2004). Sullivan et al. (1998) clarified that the extrema of the four  $\overline{w'\theta'}$  quadrants (upward warm:  $\overline{w'+\theta'^+}$ , downward warm:  $\overline{w'-\theta'^+}$ , upward cool:  $\overline{w'+\theta'^-}$ , downward cool:  $\overline{w'-\theta'^-}$ ) in the EZ more or less correspond to the average point of maximum  $\frac{\partial \bar{\theta}}{\partial z}$  (see  $h$  in Figure 1.3), whereas the

point of minimum  $\overline{w'\theta'}$  was consistently lower. They defined CBL height, based on local  $\frac{\partial \theta}{\partial z}$  and applied horizontal averaging, as well as in two ways based on  $\overline{w'\theta'}$  for comparison.

### 1.2.3 CBL Growth by Entrainment

The CBL grows by trapping pockets of warm stable air between or adjacent to impinging thermal plumes. Traumner et al. (2011) summarize two categories of CBL entrainment:

- Non turbulent fluid can be engulfed between or in the overturning of thermal plumes. This kind of event has been supported by the visualizations in Sullivan et al.'s (1998) LES study as well as in Traumner et al.'s (2011) observations. In both it appeared to occur under a weak inversion or upper lapse rate ( $\gamma$ )
- Impinging thermal plumes distort the inversion interface dragging wisps of warm stable air down at their edges or during recoil under a strong inversion or lapse rate. This type of event is supported by the findings of both Sullivan et al. (1998) and Traumner et al. (2011).

Shear induced instabilities do occur at the top of the atmospheric boundary layer and in some laboratory studies of turbulent boundary layers, under conditions of very high stability, breaking of internal waves have been observed. Entrainment via the former is relatively insignificant in strong convection, and the latter has not been directly observed in real or modeled atmospheric CBLs over the range of conditions considered here (Traumner et al. 2011, Sullivan et al. 1998).

### 1.2.4 The CBL Entrainment Layer (EZ)

The ML is fully turbulent but the top is characterized by stable air with intermittent turbulence due to the higher reaching thermals. Garcia and Mellado (2014) demonstrate that the EZ is subdivided in terms of length

and buoyancy scales. That is, the lower region is comprised of mostly turbulent air with pockets of stable warmer air that are quickly mixed, and so scales with the convective scales (see section 1.2.6). Whereas the upper region is mostly stable apart from the impinging thermals so scaling here is more influenced by the lapse rate ( $\gamma$ ). In the EZ the vertical heat flux,  $\overline{w'\theta'}$ , switches sign relative to that in the ML. The fast updraughts are now relatively cool  $\overline{w'+\theta'-}$ . In their analysis of the four  $\overline{w'\theta'}$  quadrants Sullivan et al. (1998) concluded that the net dynamic in this region is downward motion of warm air ( $\overline{w'-\theta'+}$ ) from the free atmosphere (FA) since the other three quadrants effectively cancel.

In terms of tracer concentration, and for example based on a Lidar backscatter profile, there are two ways to conceptually define the EZ. It can be thought of as the range in space (or time) over which local CBL height varies (Crum et al. 1987) or a local region over which the concentration (or back-scatter intensity) transitions from ML to FA values (Traumner et al. 2011). The latter can be estimated using either curve-fitting or wavelet techniques (Traumner et al. 2011, Steyn et al. 1999, Brooks and Fowler 2012).

Brooks and Fowler apply a wavelet technique to tracer profiles for the determination of EZ boundaries, in their 2012 LES study. However, it is more common in numerical modelling and laboratory studies for the EZ boundaries to be defined based on the average vertical turbulent heat flux ( $\overline{w'\theta'}$ ) i.e. the points enclosing the negative region as shown in Figure 1.3 (Deardorff et al. 1980, Federovich et al. 2004, Garcia and Mellado 2014). Bulk models based on the representation in Figure 1.3 assume the region of negative  $\overline{w'\theta'}$  coincides with the region where  $\bar{\theta}$  transitions from the ML value to the FA value (Deardorff 1979, Federovich et al. 2004) but no modelling studies use the vertical  $\bar{\theta}$  profile to define the EZ.

Since  $\bar{\theta}$  modeled by an LES is not strictly constant with respect to height in the ML (Federovich et al. 2004), a threshold value for  $\bar{\theta}$  or its vertical gradient must be chosen to identify the lower EZ boundary. In their 2012

LES study Brooks and Fowler encountered inconsistencies when determining the EZ boundaries from the average tracer profile. Although their tracer profile was quite different to a simulated CBL  $\bar{\theta}$  profile, this could serve as a cautionary note.

Our understanding of the characteristics and dynamics of the atmospheric CBL entrainment layer evolves with the increasing body of measurement (Traumner et al. 2011, Nelson et al. 1989), laboratory (Deardorff et al. 1980) and numerical studies (Deardorff 1972, Sorbjan 1996, Sullivan et al. 1998, Ebert et al. 1989, Federovich et al. 2004, Brooks and Fowler 2012, Garcia and Mellado 2014). Parameterizations for CBL growth and EZ depth are derived based on bulk models and are evaluated using LES output and measurements (Federovich et al. 2004, Boers 1989). So the relationship between theory, numerical simulation and measurement is inextricable and any study based on one must refer to at least one of the others.

### 1.2.5 Modelling the CBL and EZ

#### Bulk Models

Bulk models for the Convective Boundary layer (CBL) based on average, vertical profiles of ML quantities can be subdivided into: (i) zero order as represented in Figure 1.4 and (ii) first (and higher) order bulk models as represented in Figure 1.3. Order refers to the number of prognostic variables, and increased order corresponds to increasing complexity in the shape of the  $\bar{\theta}$  and  $\overline{w'\theta'}$  profiles at the top of the ML.

Zero-order bulk models assume an ML of uniform potential temperature ( $\bar{\theta}_{ML}$ ) topped by an infinitesimally thin layer across which there is a temperature jump ( $\delta\theta$ ) and above which is a constant lapse rate ( $\gamma$ ). The assumed vertical heat flux,  $\overline{w'\theta'}$ , decreases linearly from the surface up, reaching a maximum negative value  $(\overline{w'\theta'})_h$ . This is a constant proportion

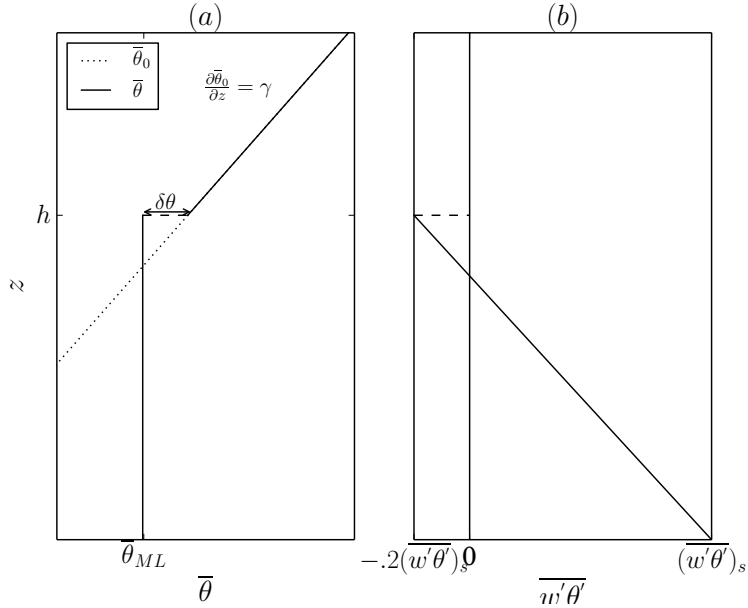


**Figure 1.4:** Simplified version of Figure 1.3 such that the EZ is infinitesimally thin. (a)  $h$  is the height of the inversion and  $\delta\theta$  the corresponding temperature jump, that is, the difference between  $\bar{\theta}_{ML}$  and  $\bar{\theta}_0(h)$ . This is different, although related, to the jump across the EZ in Figure 1.3  $\Delta\theta$ . (b) The  $w'\theta'$  profile is linear and decreasing until it reaches a maximum negative value at  $h$  of  $-.2(\bar{w}'\theta')_s$ . Here there is a discontinuity as it jumps to zero.

of the surface value, usually  $-0.2(\bar{w}'\theta')_s$  (see Section 4 in Tennekes 1973 for a discussion). At the temperature inversion  $\bar{w}'\theta'$  jumps to zero across the infinitesimally thin layer. Equations for the evolution of CBL height,  $\bar{\theta}_{ML}$  and  $\delta\theta$  are derived on this basis (Tennekes 1973).

If the CBL height ( $h$ ) is rising, air is being drawn in from the stable free atmosphere (FA) layer above and mixed with cooler air i.e. there is an overall decrease in enthalpy. The rate of decrease in enthalpy with respect to time is  $c_p\rho\delta\theta\frac{dh}{dt}$  (see Section 7.1) per unit of horizontal area where, in the absence of subsidence,  $\frac{dh}{dt}$  is the entrainment rate ( $w_e$ ). Since the lapse rate

above the inversion is stable, Tennekes (1973) equates this enthalpy loss to the average vertical turbulent heat flux at the inversion

$$\delta\theta \frac{dh}{dt} = -(\overline{w'\theta'})_h. \quad (1.1)$$

The ML warming rate is arrived at via the simplified Reynolds averaged conservation of enthalpy, for which the full derivation is shown in Section 7.3.

$$\frac{\partial \bar{\theta}_{ML}}{\partial t} = -\frac{\partial}{\partial z} \overline{w'\theta'}. \quad (1.2)$$

Assuming  $\overline{w'\theta'}$  has a constant slope this becomes

$$\frac{\partial \bar{\theta}_{ML}}{\partial t} = \frac{(\overline{w'\theta'})_s - (\overline{w'\theta'})_h}{h} \quad (1.3)$$

and the evolution of the temperature jump ( $\delta\theta$ ) depends on the rate of CBL height ( $h$ ) increase, the upper lapse rate  $\gamma$  and the ML warming rate

$$\frac{d\delta\theta}{dt} = \gamma \frac{dh}{dt} - \frac{d\bar{\theta}_{ML}}{dt}. \quad (1.4)$$

An assumption about the vertical heat flux at the inversion ( $h$ ), such as the entrainment ratio, closes this set

$$\frac{(\overline{w'\theta'})_h}{(\overline{w'\theta'})_s} = -.2. \quad (1.5)$$

The relevant quantities in equations 2.2 through 2.5 are idealized, ensemble averages. There is some variation within this class of model. For example the rate equation for  $h$  (entrainment relation) can alternatively be derived based on the turbulent kinetic energy budget (Federovich et al. 2004, Stull 1976, Stull 1976) but they are all based on the simplified  $\bar{\theta}$  and  $\overline{w'\theta'}$  profiles outlined above.

First (and higher) order models assume an EZ of finite depth at the top of

the ML, defined by two heights: the top of the ML ( $h_0$ ) and the point where FA characteristics are resumed ( $h_1$ ). The derivations are more complex and involve assumptions about the EZ i.e.:

- $\Delta h = h_1 - h_0 = \text{Constant}$  (Betts 1974)
- $\Delta h = h_1 - h_0$  is related to the zero-order jump at  $h$  by two right angled triangles with opposite sides of lengths  $h_1 - h$  and  $h - h_0$  (Batchvarova and Gryning 1994)
- $\Delta h$  or maximum overshoot distance  $d \propto \frac{w^*}{N}$  where  $w^*$  is the Deardorff convective vertical velocity scale and  $N = \sqrt{\frac{g}{\theta} \frac{\partial \theta}{\partial z}}$  is the Brunt-Vaisala frequency (Stull 1973)
- For  $h_0 < z < h_1$   $\bar{\theta} = \bar{\theta}_{ML} + f(z, t)\Delta\theta$  where  $f(z, t)$  is a dimensionless shape factor (Deardorff 1979, Federovich et al. 2004)

Although development of these models is beyond the scope of this thesis, they are mentioned to give context to the parameterizations considered in Sections 1.2.6 and 1.2.6.

## Numerical Simulations

Numerical simulation of the CBL is carried out by solving the Navier Stokes equations, simplified according to a suitable approximation, on a discrete grid. Types of simulations can be grouped according to the scales of motion they resolve. In direct numerical simulations (DNS) the full range of spatial and temporal turbulence are resolved from the size of the domain down to the smallest dissipative scales i.e. the Kolmogorov micro-scales (Kolmogorov 1962). This requires a dense numerical grid and so can be computationally prohibitive.

In an LES motion on scales smaller than twice or more of the grid spacing are filtered out and parameterized by a sub-grid scale closure model. General circulation models (GCM) solve the Navier Stokes equations on a

spherical grid and parameterize smaller-scale processes including convection and cloud cover. LES has increasingly been used to better understand the CBL since Deardorff (1972) devised this relatively new method for this purpose. Sullivan et al. (1998), Federovich et al. (2004), Ebert et al. (1989) and Brooks and Fowler in (2012) used it to study the structure and scaling behaviour of the EZ.

### 1.2.6 Scales and Scaling Relations of the CBL and EZ

#### Length Scale ( $h$ )

Deardorff (1972) demonstrated that dominant turbulent structures in penetrative convection scale with CBL height, which he referred to as the inversion height but measured as the height of minimum average vertical heat flux:  $z_f$  as shown later in Figure 1.6 (Deardorff et al. 1980). Since then, the distinction between the two has been clarified (see Section 1.2.2) and here  $h$  refers strictly to the height of maximum average potential temperature gradient. There are alternatives. For example turbulence based definitions, such as the velocity variance and the distance over which velocity is correlated with itself, represent the current turbulent dynamics rather than the recent turbulence history as does  $h$  (Traumner et al. 2011).

#### Convective Velocity Scale ( $w^*$ )

Given an average surface vertical heat flux  $(\overline{w'\theta'})_s$  a surface buoyancy flux can be defined as  $\frac{g}{\theta}(\overline{w'\theta'})_s$  which gives the convective velocity scale when multiplied by the appropriate length scale. Since the result has units  $\frac{m^3}{s^3}$  a cube root is applied

$$w^* = \left( \frac{gh}{\theta} (\overline{w'\theta'})_s \right)^{\frac{1}{3}}. \quad (1.6)$$

Deardorff (1970) confirmed that this effectively scaled the local vertical turbulent velocity fluctuations ( $w'$ ) in the CBL. ?'s (?) work supports this, even at the CBL top. The CBL entrainment rate ( $w_e = \frac{dh}{dt}$ , neglecting large scale subsidence) depends on the magnitude of  $w'$  which is driven by  $(\overline{w'\theta'})_s$ . Stability aloft suppresses  $\frac{dh}{dt}$  so the influence of  $\gamma$  is indirectly accounted for via  $h$  in  $w^*$ .

### Deardorff Convective Time Scale ( $\tau$ )

It follows that the time a thermal, travelling at velocity scaled by  $w^*$ , takes to reach the top of the CBL i.e. travel a distance  $h$  is scaled by

$$\tau = \frac{h}{\left(\frac{gh}{\theta} (\overline{w'\theta'})_s\right)^{\frac{1}{3}}}. \quad (1.7)$$

This is also referred to as the convective overturn time scale. Sullivan et al. (1998) showed a linear relationship between  $h$  and time scaled by  $\tau$ . An alternative is the Brunt-Vaisala frequency i.e. the time scale associated with the buoyant thermals overshooting and sinking (Federovich et al. 2004). The ratio of these two time-scales forms a parameter which characterizes this system (see ? ? and Deardorff 1979).

### Temperature Scales ( $\theta^*$ and $\delta h\gamma$ )

The CBL temperature fluctuations  $\theta'$  are influenced by  $\overline{w'\theta'}$  from both the surface and the CBL top. Deardorff (1970) showed that an effective scale based on the convective velocity scale is

$$\theta^* = \frac{(\overline{w'\theta'})_s}{w^*}. \quad (1.8)$$

Whereas ? (?) showed that with proximity to the CBL top the effects of FA stability  $\gamma$  become more important.

I introduce an alternative potential temperature scale for the EZ ( $\delta h\gamma$ ) in Figure 1.5. This is the difference in the initial or background potential temperature ( $\bar{\theta}_0$ ) across the upper part of the EZ, i.e. between  $h$  and  $h_1$ .

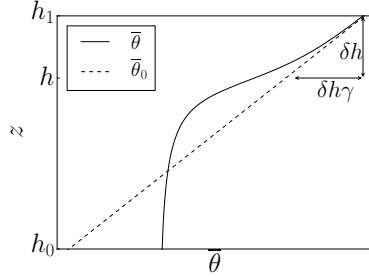


**Figure 1.5:** Representation of the  $\bar{\theta}_0$  difference across the upper part of the EZ,  $\delta h\gamma$  where  $\delta h = h_1 - h$ . This serves as an alternative to the convective potential temperature scale  $\theta^*$ .

### Buoyancy Richardson Number (Ri)

The flux Richardson ( $R_f$ ) number expresses the balance between mechanical and buoyant production of turbulent kinetic energy (TKE) and is obtained from the ratio of these two terms in the TKE budget equation (See Appendix, Stull 1988):

$$R_f = \frac{\frac{g}{\theta} (\overline{w' \theta'})_s}{\overline{u'_i u'_j \frac{\partial U_i}{\partial x_j}}}. \quad (1.9)$$

Assuming horizontal homogeneity and vertically constant subsidence yields

$$R_f = \frac{\frac{g}{\theta} (\overline{w' \theta'})}{\overline{u' w' \frac{\partial U}{\partial z}} + \overline{v' w' \frac{\partial V}{\partial z}}}. \quad (1.10)$$

Applying first order closure to the flux terms, i.e. assuming they are proportional to the vertical gradients, gives the gradient Richardson number ( $R_g$ )

$$R_g = \frac{\frac{g}{\theta} \frac{\partial \bar{\theta}}{\partial z}}{\left( \frac{\partial \bar{U}}{\partial z} \right)^2 + \left( \frac{\partial \bar{V}}{\partial z} \right)^2}, \quad (1.11)$$

However, in the EZ buoyancy acts to suppress buoyant production of TKE. Applying a bulk approximation to the denominator, and expressing it in terms of scales yields a squared ratio of two time scales

$$R_g = \frac{\frac{g}{\theta} \frac{\partial \bar{\theta}}{\partial z}}{\frac{V^{*2}}{L^2}} = N^2 \frac{L^2}{V^{*2}}, \quad (1.12)$$

where  $V^*$  and  $L^*$  are appropriate velocity and length scales. Applying the bulk approximation to both the numerator and denominator yields the bulk Richardson number:

$$R_b = \frac{\frac{g}{\theta} \Delta \theta L^*}{V^{*2}}. \quad (1.13)$$

A natural choice of length and velocity scales for the CBL are  $h$  and  $w^*$  giving the convective or buoyancy Richardson number:

$$Ri = \frac{\frac{g}{\theta} \Delta \theta h}{w^{*2}}. \quad (1.14)$$

Where  $\Delta \theta$  can be replaced by  $\delta \theta$  as in Federovich et al. (2004) and Garcia and Mellado (2014).  $Ri$  can also be arrived at by considering the principal forcings of the system, or from non-dimensionalizing the entrainment relation derived analytically (Tennekes 1973, Deardorff 1972). It is central to any study on CBL entrainment (Sullivan et al. 1998, Federovich et al. 2004, Traumner et al. 2011, Brooks and Fowler 2012).

### **Relationship of Entrainment Layer Depth to Richardson Number**

A relationship of the scaled entrainment layer EZ depth to  $Ri$

$$\frac{\Delta h}{h} \propto Ri^b \quad (1.15)$$

is arrived at by considering the deceleration of a thermal as it overshoots its

neutral buoyancy level (Nelson et al. 1989). If the velocity of the thermal is assumed to be proportional to  $w^*$  and the decelerating force is due to the buoyancy difference, or  $\theta$  jump, then the distance the thermal overshoots ( $d$ ) can be approximated by

$$d \propto \frac{w^{*2}}{\frac{g}{\bar{\theta}_{ML}} \Delta \theta}. \quad (1.16)$$

If the EZ depth is proportional to the overshoot distance ( $d$ ) then

$$\frac{\Delta h}{h} \propto \frac{w^{*2}}{\frac{g}{\bar{\theta}_{ML}} \Delta \theta h} = Ri^{-1}. \quad (1.17)$$

Alternatively, Boers 1989 integrated the internal ( $U$ ), potential ( $P$ ) and kinetic ( $K$ ) energy over a hydrostatic atmosphere

$$U = \frac{c_v}{g} \int_0^{p_0} T dp. \quad (1.18)$$

$$P = \frac{R}{c_v} U, \quad (1.19)$$

and

$$K = \frac{1}{2} \int_0^{p_0} \frac{w^2}{g} dp. \quad (1.20)$$

$p_0$  is the surface pressure,  $R$  and  $c_v$  are the gas constant and heat capacity of dry air at constant volume.  $T$  is temperature. Initially there is a flat infinitesimally thin inversion interface which is distorted by an impinging thermal. The resulting height difference is assumed sinusoidal and an average  $\Delta h$  is obtained by integrating over a wavelength. At this point, no entrainment is assumed to have occurred and all of the initial kinetic energy ( $K_i$ ) has been transferred to the change in potential energy ( $\Delta P$ ).

$$K_i = P_f - P_i = \Delta P \quad (1.21)$$

Assuming a dry adiabatic atmosphere and that the vertical velocity in the layer below the inversion can be approximated by the convective velocity

scale ( $w^*$ ), the following expression is reached

$$\left(\frac{\Delta h}{h}\right)^2 \propto \frac{T_0 w^{*2}}{g \Delta \theta h}. \quad (1.22)$$

The reference temperature,  $T_0$ , can be replaced by  $\bar{\theta}_{ML}$  to give

$$\frac{\Delta h}{h} \propto Ri^{-\frac{1}{2}} \quad (1.23)$$

### Relationship of Entrainment Rate to Richardson Number

The relationship between scaled entrainment rate and the buoyancy Richardson number (Ri)

$$\frac{w_e}{w^*} \propto Ri^a \quad (1.24)$$

is arrived at according to the zero order bulk model through thermodynamic arguments, or by integration of the conservation of enthalpy or turbulent kinetic energy equations over the growing CBL. (Tennekes 1973, Deardorff 1979, Federovich et al. 2004). It has been verified in numerous laboratory and numerical studies (Deardorff et al. 1980, Sullivan et al. 1998, Federovich et al. 2004, Brooks and Fowler 2012), but there is still some unresolved discussion as to the exact value of  $a$ . It seems there are two possible values,  $-\frac{3}{2}$  and  $-1$ , the first of which Turner (1986) suggested occurs at high stability when buoyant recoil of impinging thermals becomes more important than their convective overturning. Assume that an impinging thermal supplies kinetic energy ( $K$ ) per unit time and per unit area for entrainment, in terms of appropriate length and time scales  $L^*$  and  $t^*$  as follows

$$K \propto \frac{\bar{\rho} L^{*3} U^{*2}}{L^{*2} t^*}, \quad (1.25)$$

and that the corresponding change in potential energy per unit time and area of the rising CBL is

$$\Delta P \propto g \Delta \rho h \frac{dh}{dt}. \quad (1.26)$$

If  $L^*$  is the penetration depth of the thermals travelling at velocity scaled by  $w^*$  against a decelerating force  $g\frac{\Delta\rho}{\bar{\rho}}$

$$L^* = \frac{w^{*2}\bar{\rho}}{\Delta\rho}. \quad (1.27)$$

where  $\frac{\bar{\rho}}{\Delta\rho}$  can be replaced with  $\frac{\bar{\theta}}{\Delta\theta}$  or  $\frac{\bar{\theta}}{\delta\theta}$  (see Stull (1988) pg 80 and Section 7.1) and  $t^*$  is the response time of the inversion layer to a thermal of length  $h$

$$t^* = \sqrt{h\frac{\bar{\theta}}{g\Delta\theta}} \quad (1.28)$$

then assuming all of  $K$  is transferred to the change in potential energy ( $\Delta P$ ) and using the convective velocity scaled, yields

$$\frac{\frac{dh}{dt}}{w^*} \propto \frac{\bar{\theta}w^{*2}}{g\Delta\theta h} \sqrt{\frac{\bar{\theta}w^{*2}}{g\Delta\theta h}}, \quad (1.29)$$

i.e.

$$\frac{w_e}{w^*} \propto Ri^{-\frac{3}{2}}. \quad (1.30)$$

Adding further complexity to this discussion, Federovich et al. (2004) suggest that this power law relationship ( $a = -\frac{3}{2}$ ) can be arrived at through defining the  $\theta$  jump across the EZ rather than at  $h$  (see Figure 1.3).

### 1.3 Research Questions

A simplified conceptual model of the dry, shear-free CBL in the absence of large scale winds is represented in Figure 1.3. The two principal external parameters in this case, are the average vertical turbulent surface heat flux ( $\overline{w'\theta'}$ )<sub>s</sub> and the upper lapse rate ( $\gamma$ ) (Federovich et al. 2004,? ?). They have opposing effects, that is to say ( $\overline{w'\theta'}$ )<sub>s</sub> drives upward turbulent velocity ( $w'^+$ ) and so CBL growth ( $w_e$ ) whereas  $\gamma$  suppresses it. Conversely they both cause positive turbulent potential temperature fluctuations ( $\theta'^+$ )

and so warming of the CBL. In the EZ the thermals from the surface are now relatively cool. They turn downwards as they interact with the stable FA concurrently bringing down warmer air. Sullivan et al. (1998) demonstrated these dynamics by partitioning  $\overline{w'\theta'}$  into four quadrants. ? (?) asserted and showed that in this region the turbulent potential temperature fluctuations ( $\theta'$ ) are strongly influenced by  $\gamma$  whereas the turbulent vertical velocity fluctuations ( $w'$ ) are almost independent thereof. Inspired by these two studies and to gain some insight into the dynamics of this idealized CBL I ask **Q1: How do the distributions of local CBL height, and the joint distributions of  $w'$  and  $\theta'$  within the EZ, vary with  $(\overline{w'\theta'})_s$  and  $\gamma$ ?**

The relationship between scaled EZ depth and  $Ri$

$$\frac{\Delta h}{h} \propto Ri^b \quad (1.15)$$

has been explored and justified in field measurement, laboratory and numerical studies. There is disagreement with respect to its exact form, in part stemming from variation in height and  $\theta$  jump definitions, but in general its magnitude relative to  $h$  decreases with increasing  $Ri$ . Although referred to in most relevant studies and relied upon in analytical models, the vertical average potential temperature profile has not been used to define the EZ (Deardorff et al. 1980, Nelson et al. 1989, Federovich et al. 2004, Boers 1989, Brooks and Fowler 2012). This leads me to ask **Q2: Can the EZ boundaries be defined based on the  $\bar{\theta}$  profile and what is the relationship of the resulting depth ( $\Delta h$ ) to  $Ri$ ?**

A further simplification to the dry, shear-free, CBL model without large scale velocities, is to regard the EZ depth as infinitesimally small as in Figure 1.4. The relationship of the scaled, time rate of change of  $h$  (entrainment rate:  $w_e$ ) to  $Ri$  can be derived based on this model (Tennekes 1973, Deardorff 1979, Federovich et al. 2004)

$$\frac{w_e}{w^*} \propto Ri^a. \quad (1.24)$$

This will be referred to as the entrainment relation. Although that there is such a relationship is well established, discussion as to the power exponent of  $Ri$  is unresolved and results from studies justify values of both  $-\frac{3}{2}$  and  $-1$ . See Traumner et al. (2011) for a summary and review. Turner (1986) explains this disparity in terms of entrainment mechanism such that the higher value occurs when thermals recoil rather than overturn in response to a stronger  $\theta$  jump (or inversion). Whereas Sullivan et al. (1998) notice a deviation from the lower power ( $-1$ ) at lower  $Ri$  and attribute it to the effect of a the shape of  $\bar{\theta}$  within a thicker EZ. Both Federovich et al. (2004) and Garcia and Mellado (2014) show how the definition of the  $\theta$  jump influences the time rate of change of  $Ri$  and so effects  $a$ . **Q3: How does defining the  $\theta$  jump based on the vertical  $\bar{\theta}$  profile across the EZ as in Figure 1.3 vs at the inversion ( $h$ ) as in Figure 1.4, affect the entrainment relation and in particular  $a$ ?**

## 1.4 Approach to Research Questions

### General Setup

I modelled the dry shear free CBL and EZ using LES, specifically the cloud resolving model System for Atmospheric Modelling (SAM) to be outlined in Chapter 3. An ensemble of 10 cases was run to obtain true ensemble averages and turbulent potential temperature variances ( $\theta'$ ), each case had a domain of area  $3.2 \times 4.8 \text{ Km}^2$ . Grid spacing was influenced by the resolution study of Sullivan and Patton (2011) and the vertical grid within the EZ was of higher resolution than that applied in other comparable work. The runs were initialized with a constant  $(\overline{w'\theta'})_s$  acting against a uniform  $\gamma$ . So, the  $\theta$  jump arose from the overshoot of the thermals, rather than being initially imposed as in Sullivan et al. (1998) and Brooks and Fowler (2012).

## Verifying Output

Before addressing the questions stated in Section 1.3 I will examine the modeled output to make sure it represents a realistic turbulent CBL in Chapter 3 section 2. I will verify that the averaged vertical profiles are as expected and coherent thermals are being produced. FFT energy density spectra will show if there is adequate scale separation between the structures of greatest energy and the grid spacing, and that realistic, isotropic turbulence is being modelled.

## Q1 Entrainment Zone Structure

The EZ can be thought of in terms of the distribution of individual thermal heights, or local heights. Sullivan et al. (1998) measured local height by locating the vertical point of maximum  $\theta$  gradient, and observed the effects of varying  $Ri$  on the resulting distributions. However this method is problematic when gradients in the upper profile exceed that at the inversion (Brooks and Fowler 2012). Steyn et al. (1999) fitted an idealized curve to a Lidar backscatter profile. This method produces a smooth curve based on the full original profile on which a maximum can easily be located. I will apply a multi-linear regression method outlined in Vieth (2011) to the local  $\theta$  profile, representing the ML, EZ and FA each with a separate line segment. From this fit, I will locate the ML top ( $h_0^l$ ). I'll observe how the resulting distributions are effected by changes in  $(\overline{w'\theta'})_s$  and  $\gamma$  using histograms in Chapter 3 Section 3.

Sullivan et al. (1998) broke  $w'\theta'$  into four quadrants and used this combined with local flow visualizations to show how CBL thermals impinge and draw down warm air from above. Mahrt and Paumier (1984) used 2 dimensional contour plots of local  $w'$  and  $\theta'$  measurements to analyze their joint distributions. In his ? LES study ? showed that in the EZ,  $\theta'$  is strongly influenced by  $\gamma$  whereas  $w'$  is independent thereof. Influenced by these three studies, I will use 2 dimensional histograms at  $h$  and so within the EZ to look at how the distributions of local  $w'$  and  $\theta'$  are effected by changes in  $\gamma$  and  $(\overline{w'\theta'})_s$

. I will magnify the effects of  $\gamma$ , by applying the convective scales,  $\theta^*$  and  $w^*$  and hone in specifically on the entrained air at  $h$  in Chapter 3 Section 4.

## Q2 Entrainment Zone Boundaries

Here I define the CBL height as the location of maximum vertical  $\bar{\theta}$  gradient as in Figure 1.6. The lower and upper EZ boundaries are then the points at which  $\frac{\partial \bar{\theta}}{\partial z}$  significantly exceeds zero and where it resumes  $\gamma$ . The lower boundary requires choice of a threshold value which should be small, positive and less than  $\gamma$ . Since it is somewhat arbitrary I will compare results based on three different threshold values in Chapter 3 section 5. Federovich et al. (2004) and Brooks and Fowler (2012) defined the EZ in terms of the vertical  $\overline{w'\theta'}$  profiles as in Figure 1.6 but disagreed on the shape of the relationship of scaled EZ depth to  $Ri$ (equation 2.1). As well as observing this relationship using the height definitions based on the  $\bar{\theta}$  profile, I will apply the definitions based on the  $\overline{w'\theta'}$  profile for comparison with Brooks and Fowler (2012) and Federovich et al. (2004) in Chapter 3 section 4.

**Table 1.1:** Definitions based on the vertical  $\bar{\theta}$  profile in Figure 1.6. To obtain those based on the  $\overline{w'\theta'}$  profile, replace  $h_0$ ,  $h$  and  $h_0$  with  $z_{f0}$ ,  $z_f$  and  $z_{f1}$

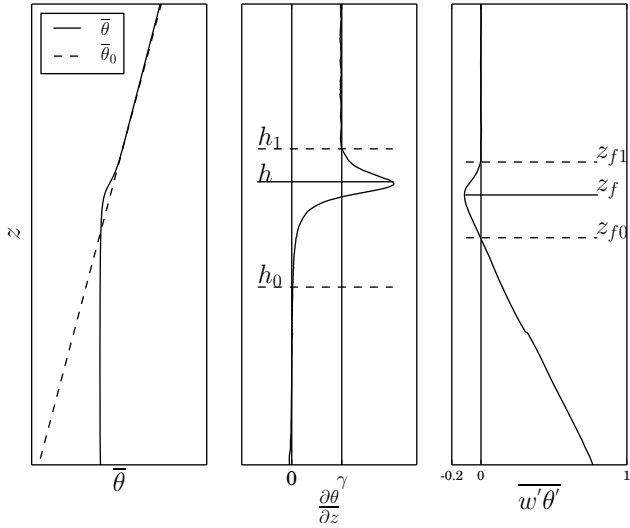
CBL Height	ML $\bar{\theta}$	$\theta$ Jump	$Ri$
$h$	$\bar{\theta}_{ML} = \frac{1}{h} \int_0^h \bar{\theta}(z) dz$	$\Delta\theta = \bar{\theta}(h_1) - \bar{\theta}(h_0)$	$Ri_\Delta = \frac{\frac{g}{\bar{\theta}_{ML}} \Delta\theta h}{w^{*2}}$

	$\delta\theta = \bar{\theta}_0(h) - \bar{\theta}_{ML}$	$Ri_\delta = \frac{\frac{g}{\bar{\theta}_{ML}} \delta\theta h}{w^{*2}}$
--	--	---

## Q3 Entrainment Rate Parameterization

As discussed in see Section 1.2.6 the form of the entrainment relation is thought to vary based on the mechanism that initiates entrainment, which



**Figure 1.6:** Height definitions based on the average vertical profiles.  
 $\theta_0$  is the initial potential temperature.

in turn depends on the magnitude of  $Ri$ . Furthermore the ways in which the height and  $\theta$  jump are defined have an effect. I will vary the definition of the  $\theta$  jump as outlined in Table 4.1 in order to discern between how this, and variation in initial conditions, influence the entrainment relation and in particular  $a$ . I will reproduce this analysis using height definitions based on  $\overline{w'\theta'}$  for comparison with the results of Federovich et al. (2004).

## 2. Tools

### 2.1 Large Eddy Simulation

System for Atmospheric Modelling (SAM) is a Large Eddy Simulation with cloud resolving capability (Khairoutdinov and Randall 2003). The dynamical framework uses the anelastic equations of motion, which in tensor notation are:

$$\frac{\partial u_i}{\partial t} = -\frac{1}{\bar{\rho}} \frac{\partial}{\partial x_i} (\bar{\rho} u_i u_j + \tau_{ij}) - \frac{\partial}{\partial x_i} \frac{p'}{\bar{\rho}} + \delta_{i3} B + \epsilon_{ij3} f (u_j - U_g j) + \left( \frac{\partial u_i}{\partial t} \right)_{l.s.} \quad (2.1)$$

and

$$\frac{\partial}{\partial x_i} \bar{\rho} u_i = 0 \quad (2.2)$$

The over-bar denotes the horizontal average and prime denotes fluctuations from the average.  $B$  is buoyancy  $= -g \frac{\rho'}{\rho}$ ,  $U_g$  is the prescribed geostrophic wind and  $f$  is the Coriolis parameter.  $\tau_{ij}$  is the sub-grid scale stress tensor and the subscript  $l.s.$  denotes the prescribed large scale tendency.

The prognostic thermodynamical variable is the liquid water/ice moist static energy ( $h_L$ ).

$$\frac{\partial h_L}{\partial t} = -\frac{1}{\bar{\rho}} \frac{\partial}{\partial x_i} (\bar{\rho} u_i h_L + F_{h_L i}) - \frac{1}{\bar{\rho}} \frac{\partial}{\partial z} (L_c P_r + L_s P_s + L_s P_g) + \left( \frac{\partial h_L}{\partial t} \right)_{rad} + \left( \frac{\partial h_L}{\partial t} \right)_{mic} \quad (2.3)$$

$L_c$  and  $L_s$  are the latent heats of condensation and sublimation.  $P_r$ ,  $P_s$  and  $P_g$  are precipitation fluxes of rain, snow and graupel. These terms reduce to zero in the absence of condensed water and precipitation. The liquid/ice water static energy is

$$h_L = c_p T + gz - L_c(q_c + q_r) - L_s(q_i + q_s + q_g) \quad (2.4)$$

where  $q_c$ ,  $q_r$ ,  $q_i$ ,  $q_s$  and  $q_g$  are the mixing ratios for cloud water, rain, ice, snow and graupel. Again, these reduce to zero in the absence of condensed water. Temperature and potential temperature are diagnosed based on this variable, at each time-step. A simple first-order Smagorinski closure scheme is used to parameterize the sub-grid stresses and scalar fluxes. The eddy diffusivity coefficient is based on the grid scale.

The model equations are represented discretely on a fully staggered Arakawa C-type grid which is uniform in the horizontal and stretched in the vertical. Integration is performed using a third-order Adams-Basforth scheme with variable time step. Momentum is advected in flux form with second order differencing and conservation of kinetic energy. Prognosed scalars are advected using a three dimensional positive definite, monotonic scheme. Lateral boundaries are periodic. The top is bounded by a rigid lid, and Newtonian damping is applied in the top third of the domain to reduce the effects of gravity waves. Surface fluxes are computed using Monin-Obukhov similarity.

## 2.2 Handling of Output

The model was run on parallel computers in a Linux environment using Message Passing Interface (MPI). 3d variable fields were output every 10 - 15 minutes in binary form and converted to Network Common Data Form (NetCDF). The use of Python was enabled using the netcdf4 interface. Plotting was done using matplotlib. All analysis, except for the tri-linear regression method for determining local ML height, were performed using NumPy

and SciPy.

### 2.2.1 Tri-Linear Fit for Determining local ML height $h_0^l$

The following is a modified version of the piecewise linear regression method used in Vieth (2011) and was implemented using Cython. Potential temperature is assumed to be linear function of height

$$\theta = bz + a \quad (2.5)$$

Each local  $\theta$  profile was assumed to have three linear portions, with slopes ( $b_1, b_2, b_3$ ) and intercepts ( $a_1, a_2, a_3$ ) as follows:

$$b_1 = \frac{\sum_0^j z(i)\theta(i) - \frac{1}{j} \sum_0^j z(i) \sum_0^j \theta}{\sum_0^j z(i)^2 - \frac{1}{j} (\sum_0^j z(i))^2} \quad (2.6)$$

$$a_1 = \frac{\sum_0^j z(i)\theta(i)}{\sum_0^j z(i)} - b_1 \frac{\sum_0^j z(i)^2}{\sum_0^j z(i)} \quad (2.7)$$

$$b_2 = \frac{\sum_j^k z(i)\theta(i) - (k-j)a_1 + b_1 z(j)}{\sum_j^k z(i) - (k-j)z(j)} \quad (2.8)$$

$$a_2 = \frac{\sum_j^k z(i)\theta(i)}{\sum_j^k z(i)} - b_2 \frac{\sum_j^k z(i)^2}{\sum_j^k z(i)} \quad (2.9)$$

$$b_3 = \frac{\sum_k^n z(i)\theta(i) - (k-j)a_1 + b_1 z(j)}{\sum_j^k z(i) - (k-j)z(j)} \quad (2.10)$$

$$a_3 = \frac{\sum_k^n z(i)\theta(i)}{\sum_k^n z(i)} - b_3 \frac{\sum_k^n z(i)^2}{\sum_k^n z(i)} \quad (2.11)$$

where  $z(i)$  and  $\theta(i)$  are a local height and potential temperature value at a particular height index  $i$ .  $j$  is the height index of the ML top,  $h_0$ .  $k$  is the height index for the top of the EZ,  $h_0$ .  $n$  is the total number of height levels. The best fit is that with the smallest residual sum of squares

$$RSS(j, k) = \sum_0^j (\theta(i) - (a_1 + b_1 z(i)))^2 + \sum_j^k (\theta(i) - (a_2 + b_2 z(i)))^2 + \sum_k^n (\theta(i) - (a_3 + b_3 z(i)))^2 \quad (2.12)$$

## 3. Output Verification

In Section ?? vertical profiles of the ensemble and horizontally averaged potential temperature and heat flux ( $\bar{\theta}$  and  $\overline{w'\theta'}$ ) will be examined for the development of the expected three layer structure (ML, EZ and FA). In order to verify that there is sufficient scale separation between the energy containing turbulent structures and the grid size and so an adequate inertial subrange, FFT energy spectra of the turbulent velocity fluctuations will be plotted. To convince the reader (and myself) that multiple coherent thermals are being produced, 2 dimensional visualizations will be shown at the three heights:  $h_0$ ,  $h$  and  $h_1$  as shown in Figure 1.6.

### 3.1 Initialization and Spin-Up Time

All 10 member cases of the ensemble were run on a 3.2 x 4.8 Km horizontal domain ( $\Delta x = \Delta y = 25m$ ,  $nx = 128$ ,  $ny = 192$ ). Grid numbers  $nx$ ,  $ny$  were chosen based on the optimal distribution across processor nodes. The vertical grid ( $nz = 312$ ) was of higher resolution around the entrainment layer ( $\Delta z = 5m$ ), lower below ( $\Delta z = 25m$ ) and stretched above it ( $\Delta z = 10$  to  $100m$ ). This was guided by Sullivan and Patton's 2011 LES resolution study of the CBL that showed how grid size affects; the shapes of the average profiles in particular around the EZ, as well as the extent of the inertial turbulence scale sub-range. The 7 runs, summarized in Table 3.1 , are all initialized with a constant surface heat flux (  $(\overline{w'\theta'})_s$  ) acting against a uniform initial lapse rate ( $\gamma$ ) and differ from each other based on these two external parameters.

$\overline{w'\theta'_s} / \gamma$	10 (K/Km)	5 (K/Km)	2.5 (K/Km)
150 (W/m2)	▼ 150/10	● 150/5 <sup>1</sup>	
100 (W/m2)	▼ 100/10	● 100/5	
60 (W/m2)	▼ 60/10	● 60/5	★ 60/2.5

**Table 3.1:** Runs in terms of  $\overline{w'\theta'_s}$  and initial lapse rate  $\gamma$

Time must be allowed for statistically steady turbulent flow to be established. Sullivan et al. (1998) recommended 10 eddy turnover times based on the convective time scale  $\tau = \frac{h}{w^*} = \frac{h}{\left(\frac{gh}{\bar{\theta}_{ML}} \overline{(w'\theta'_s)}\right)^{\frac{1}{3}}}$ , and Brooks and Fowler (2012) chose a simulated time of 2 hours. Figure 3.1 shows that for all of the runs, at least 10 eddy turnover times were completed by 2 simulated hours. Although each run has a distinct convective velocity scale  $w^*$ , that increases with time, dividing boundary layer height ( $h$ ) by it to obtain  $\tau$  results in a collapse from 7 to 3 curves, one for each  $\gamma$ .

Figure 3.2 shows that by at hours there is a measurable well mixed layer (ML) where: (i) the horizontally and ensemble averaged potential temperature ( $\bar{\theta}$ ) is constant, (ii) its vertical gradient  $\frac{\partial \bar{\theta}}{\partial z}$  is close to zero and (iii) the vertical heat flux  $\overline{w'\theta'}$  is positive and linearly decreasing. Above it is an EZ where the  $\bar{\theta}$  profile transitions through a maximum to the upper lapse rate  $\gamma$  and  $\overline{w'\theta'}$  is negative. At 3 hours the EZ is fully contained within the vertical region of high resolution in all runs. Figure 3.3 shows that the  $\overline{w'\theta'}$  profiles are similar and are scaled well by the surface heat flux (  $(\overline{w'\theta'})_s$  ) from 2 hours on.

---

<sup>1</sup>Incomplete run: EZ exceeded high resolution vertical grid after 7 hours

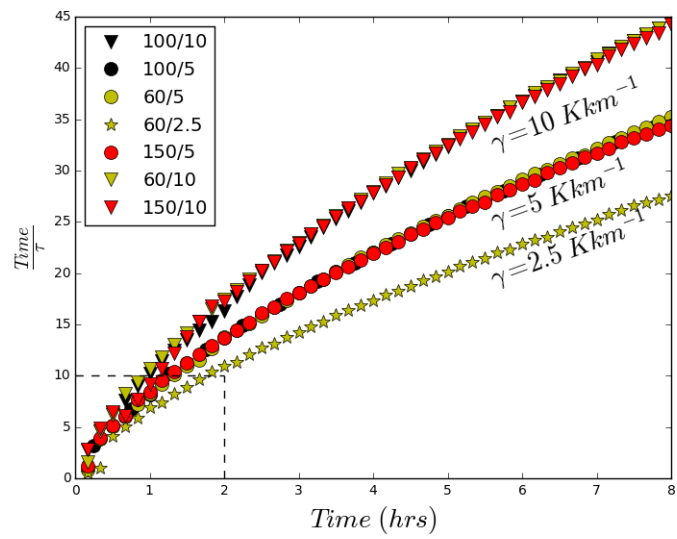


**Figure 3.1:** Plots of scaled time vs time for all runs. Scaled time is based on the convective time scale  $\tau$  and can be thought of as the number of times an eddy has reached the top of the CBL.

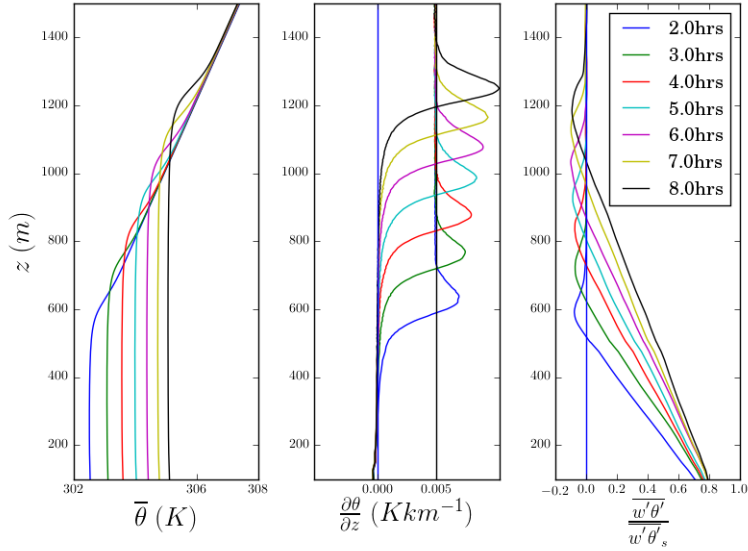


**Figure 3.2:** Vertical profiles of the horizontally and ensemble averaged potential temperature ( $\bar{\theta}$ ), its vertical gradient ( $\frac{\partial \bar{\theta}}{\partial z}$ ) and vertical heat flux ( $\overline{w' \theta'}$ ) for the 100/5 run

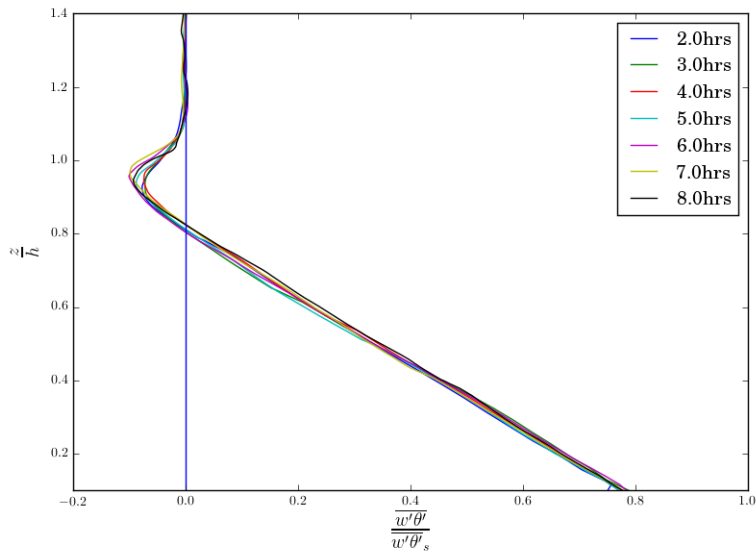


**Figure 3.3:**  $\overline{w' \theta'}$  and scaled  $\overline{w' \theta'}$  vs scaled height for the 100/5 run

### 3.2 Horizontally and ensemble averaged Potential Temperature $\bar{\theta}$ and Heat Flux $\overline{w'\theta'}$ Profiles

In Figures 3.2 and 3.4 the  $\bar{\theta}$  profiles exhibit an ML above which  $\frac{\partial \bar{\theta}}{\partial z} > 0$  and reaches a maximum value at  $h$  before resuming  $\gamma$  at  $h_1$ . Convective boundary layer CBL growth is stimulated by  $(\overline{w'\theta'})_s$  and inhibited by  $\gamma$ .

In Figures 3.2 and 3.5 the  $\overline{w'\theta'}$  profiles decrease from the surface value,  $(\overline{w'\theta'})_s$ , passing through zero to a minimum before increasing to zero. They are similar across runs when scaled by  $(\overline{w'\theta'})_s$ . All minima are less in magnitude than the zero order approximation,  $-.2 \times (\overline{w'\theta'})_s$  (Tennekes 1973), but increase with increased  $\gamma$ .

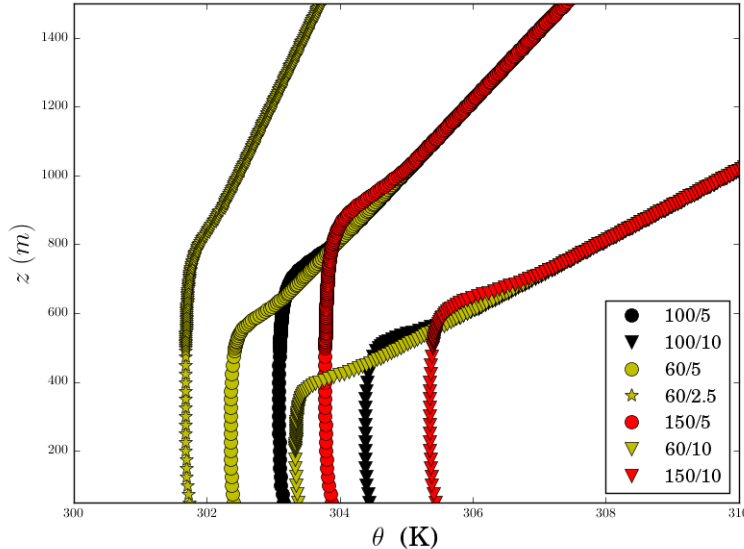


**Figure 3.4:**  $\bar{\theta}$  profiles at 2 hours for all runs

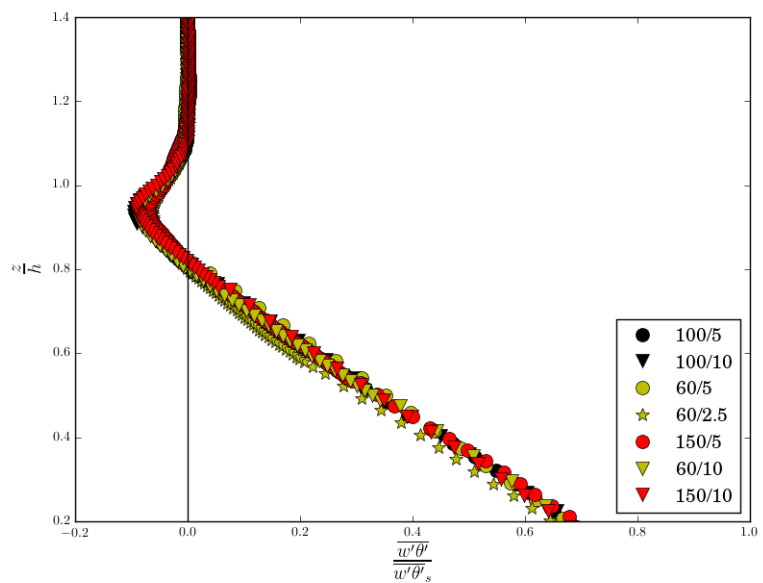


**Figure 3.5:** Scaled  $(\overline{w'\theta'})_s$  profiles at 3 hours for all runs

### 3.3 FFT Energy Spectra

In Figure 3.6, two dimensional FFT power spectra of horizontal  $w'$  slices taken at three different levels ( $h_0$ ,  $h$  and  $h_1$  as shown in Figure 1.6) are collapsed to one dimension by integrating around a circle of wave-numbers. Isotropy in all radial directions is assumed and  $k = \sqrt{k_x^2 + k_y^2}$ . The resulting scalar density spectra show peaks in energy at the larger scales, cascading through a substantial inertial subrange to the lower scales roughly according to a  $-\frac{5}{3}$  slope, lower in the EZ. At the top of the EZ where turbulence is suppressed by stability, the slope is steeper. The peak in energy occurs at smaller scales at  $h$  as compared to at  $h_0$ , indicating a change in the size of the dominant turbulent structures. The spectra for the horizontal turbulent velocity fluctuations were analogous but show lower energy as expected. All runs produced spectra with these characteristics.

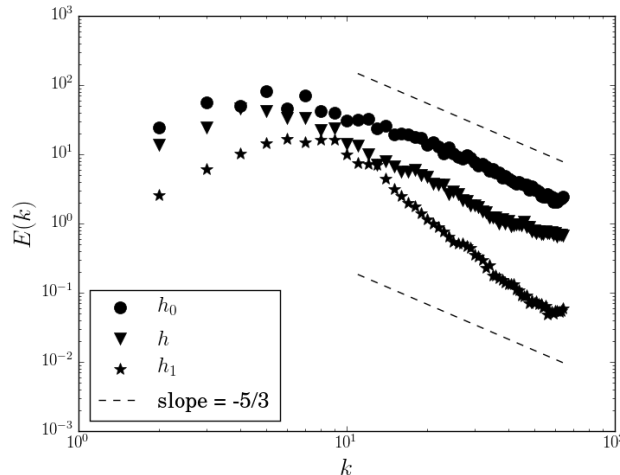


**Figure 3.6:** Scalar FFT energy vs wavenumber ( $k = \sqrt{k_x^2 + k_y^2}$ ) for the 60/2.5 run at 2 hours, taken at three heights ( $h_1$ ,  $h$  and  $h_0$ ).  $E(k)$  is  $E(k_x, k_y)$  integrated around a circle of radius  $k$ .  $E(k_x, k_y)$  is the total integrated energy over the 2D domain.  $k_x$  and  $k_y$  are number of waves per domain length.

### 3.4 Visualization of Structures within the Entrainment Zone

Horizontal slices, at  $h_0$ ,  $h$  and  $h_1$  of the potential temperature and vertical velocity fluctuations ( $\theta'$  and  $w'$ ) are plotted to see the turbulent structures. Figure 3.7 shows the bottom of the EZ ( $h_0$ ) for the 150/10 run where coherent areas of positive and negative temperature fluctuations correspond to areas of upward and downward moving air. In (b) and (e) the individual thermals of relatively cool air are more evident at the inversion ( $h$ ) and their locations correspond to areas of upward motion. Most of the upward moving cool areas are adjacent to and even encircled by smaller areas of downward moving warm air. At  $h_1$  ((c) and (f)) peaks of cool air are associated with both up and down-welling.

### 3.5 Summary of Findings

Each 10 member ensemble run was allowed a period of time to develop the three layer structure (ML, EZ and FA) as seen from the average potential temperature ( $\bar{\theta}$ ) and vertical heat flux ( $\overline{w'\theta'}$ ) profiles. The convective time scale ( $\tau$ ) for a thermal to reach the CBL top ( $h$ ) was seen to depend on  $\gamma$ , signalling the importance of this external parameter. FFT spectra of turbulent velocity fluctuations the ML showed a satisfactory inertial subrange and several coherent impinging thermals were observed in the EZ at any given time after 2 hours, indicating that realistic turbulence was being simulated.

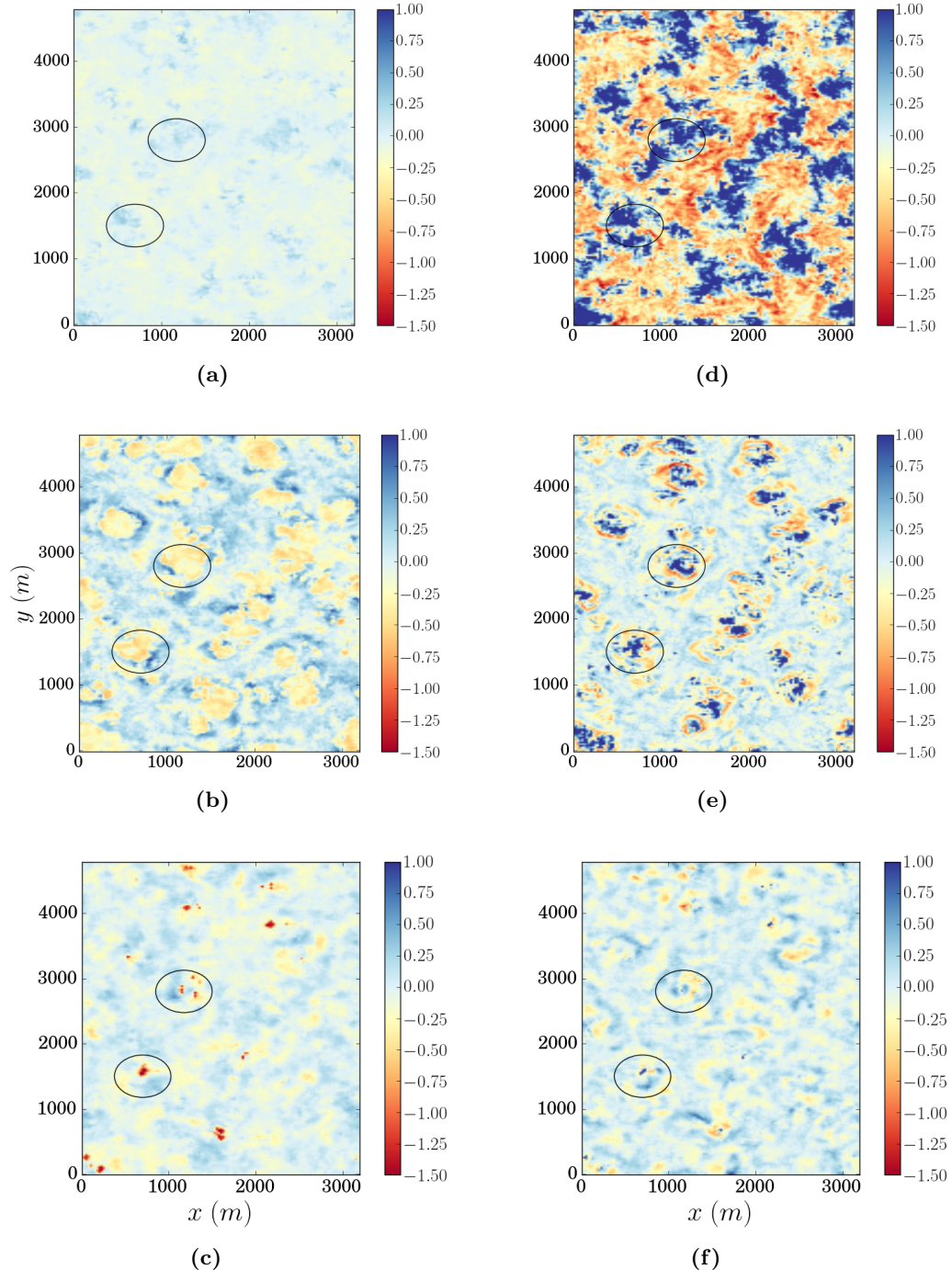


**Figure 3.7:**  $\theta'$  (left) and  $w'$  (right) at 2 hours at  $h_0$  (a,d),  $h$  (b,e) and  $h_1$  (c,f) for the 150/10 run. The locations of two impinging thermals are circled.

## 4. Research Answers

Section 4.1 will focus on answering **Q1 Entrainment Zone Structure:**

**How do the distributions of local CBL height, and the joint distributions of  $w'$  and  $\theta'$  within the EZ, vary with  $(\bar{w}'\bar{\theta}')$ <sub>s</sub> and  $\gamma$ ?**

The distributions of local ML heights at each horizontal point, in each ensemble member, will be plotted as histograms to visualize the effects of  $(\bar{w}'\bar{\theta}')$ <sub>s</sub> and  $\gamma$ . For the same reason the joint distributions of local potential temperature and velocity fluctuations ( $\theta'$  and  $w'$ ) at  $h$  will be plotted. Focus will then be narrowed to the average downward moving warm quadrant at  $h$  ( $\overline{w' - \theta'}_h^+$ ,  $\overline{w'}_h^-$  where  $\theta' > 0$  and  $\overline{\theta'}_h^+$  where  $w' < 0$ ) to examine the direct influence of  $\gamma$  on entrainment.

To answer **Q2 Entrainment Zone Boundaries:**

**Can the EZ boundaries be defined based on the  $\bar{\theta}$  profile and what is the relationship**

$$\frac{\Delta h}{h} \propto Ri^b \quad (1.15)$$

**of the resulting scaled depth ( $\frac{\Delta h}{h}$ ) to Ri?**

in Section 4.2, Equation 1.15 will be plotted using height definitions based on the  $\frac{\partial \bar{\theta}}{\partial z}$  profile as in Figure 1.6 and Table 4.1. Since the choice of a threshold to determine the lower EZ boundary is somewhat arbitrary, plots will be

reproduced using two additional values. For comparison with the results of Federovich et al. (2004) and Brooks and Fowler (2012), Equation 1.15 will be plotted using heights based on the average heat flux ( $\bar{w}'\theta'$ ) profile.

In Section 4.3 the temperature jump will be defined in four ways to answer

**Q3 Entrainment Rate Parameterization:**

**How does defining the  $\theta$  jump based on the vertical  $\bar{\theta}$  profile across the EZ as in Figure 1.3 vs at the inversion ( $h$ ) as in Figure 1.4, affect the entrainment relation**

$$\frac{w_e}{w^*} \propto Ri^a \quad (1.24)$$

**and in particular  $a$ ?**

This analysis will involve observing how CBL height evolves in time and culminate in four plots representing Equation 1.24 in log-log coordinates such that the most suitable values of the exponent  $a$  can be identified.

## 4.1 Q1 Entrainment Zone Structure

### 4.1.1 Local Mixed Layer Heights ( $h_0^l$ )

In Figures 4.1 and 4.2 the local vertical  $\theta$  profiles, each at a single horizontal point in an individual case, exhibit a distinct ML. Above, there are sharp changes in the profile well into the free atmosphere, due possibly to waves. These render the gradient method for determining a local CBL height,  $h^l$ , unreliable. Instead a linear regression method is used, whereby three lines representing: the ML, the EZ and the upper lapse rate ( $\gamma$ ), are fit to the profile according to the minimum residual sum of squares. Determining local ML height ( $h_0^l$ ) in this way was more straight forward than the local height of maximum potential temperature gradient ( $h^l$ ) for the reasons stated above.

Figure 4.1 shows two local  $\theta$  profiles where  $h_0^l$  is relatively high. A sharp interface is evident indicating that this is within an active thermal impinging on the stable layer. In Figure 4.2 where  $h_0^l$  is relatively low a less defined interface indicates a point now outside a rising thermal. Under weaker stability ( $\gamma$ ), as in Figure 4.2 (a), these inactive locations show a larger vertical region that could be called a local EZ. In two-dimensional horizontal plots, not shown here, regions of high  $h_0^l$  corresponded to regions of upward moving relatively cool air at  $h$ .

The distribution of  $h_0^l$  represents the range over which CBL height varies in space, so as discussed in Section 1.2.4, relates to the depth of the entrainment zone (EZ). Figure 4.3 (a), (b) and (c) illustrate that the distribution widens with increasing  $(\overline{w'\theta'})_s$  and narrows with increasing  $\gamma$ . When scaled by  $h$ , the local ML height distribution narrows with increased  $\gamma$ , in Figure 4.3 (d), (e) and (f). The upper boundary seems to be constant at about  $1.1(\times h)$ , whereas the lower boundary clearly increases. When  $h_0^l$ s are lower and their distribution is narrower, the scaled versions have relatively larger spacing between bins and so higher numbers in each bin. In Figure 4.3 (d),

at higher  $(w'\theta')_s$  there are fewer  $\frac{h_0^l}{h}$  values with higher probabilities, but the width of the distributions is more or less constant regardless of  $(w'\theta')_s$ .

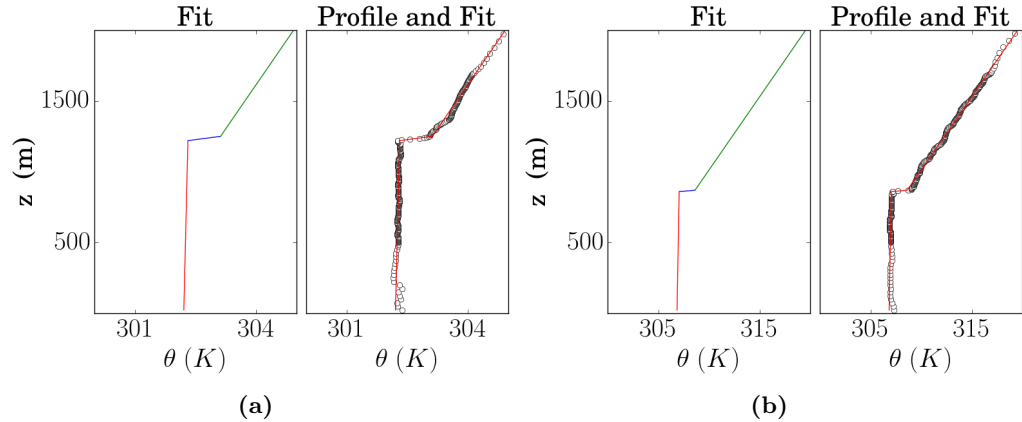


**Figure 4.1:** Local vertical  $\theta$  profiles with 3-line fit for the 60/2.5 (a) and 150/10 (b) runs at points where  $h_0^l$  is high.

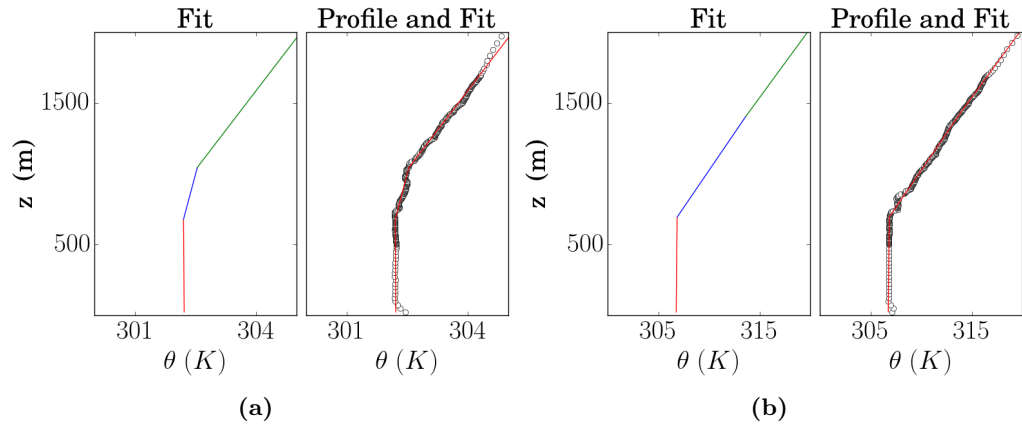


**Figure 4.2:** Local vertical  $\theta$  profiles with 3-line fit for the 60/2.5 (a) and 150/10 (b) runs at points where  $h_0^l$  is low.

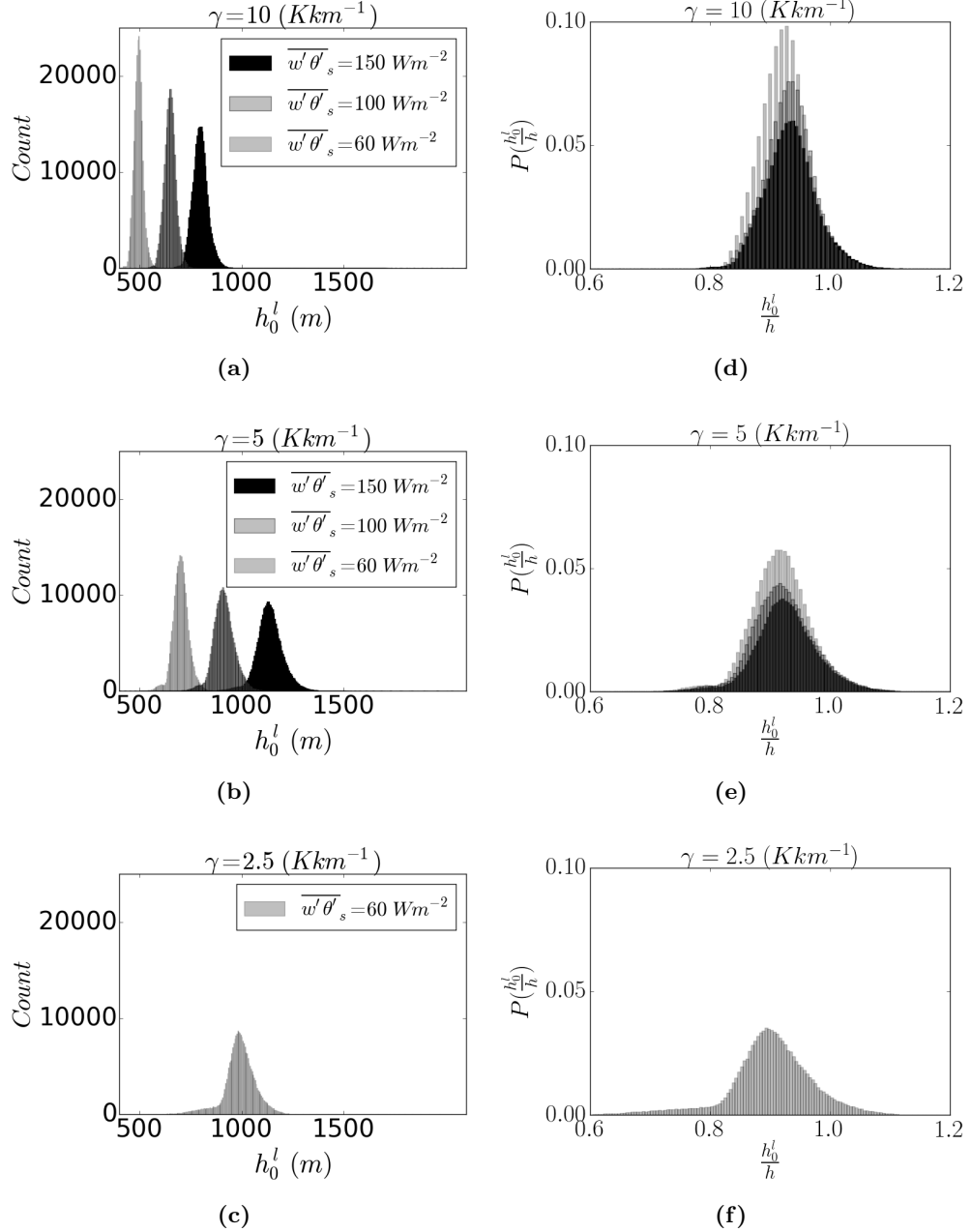


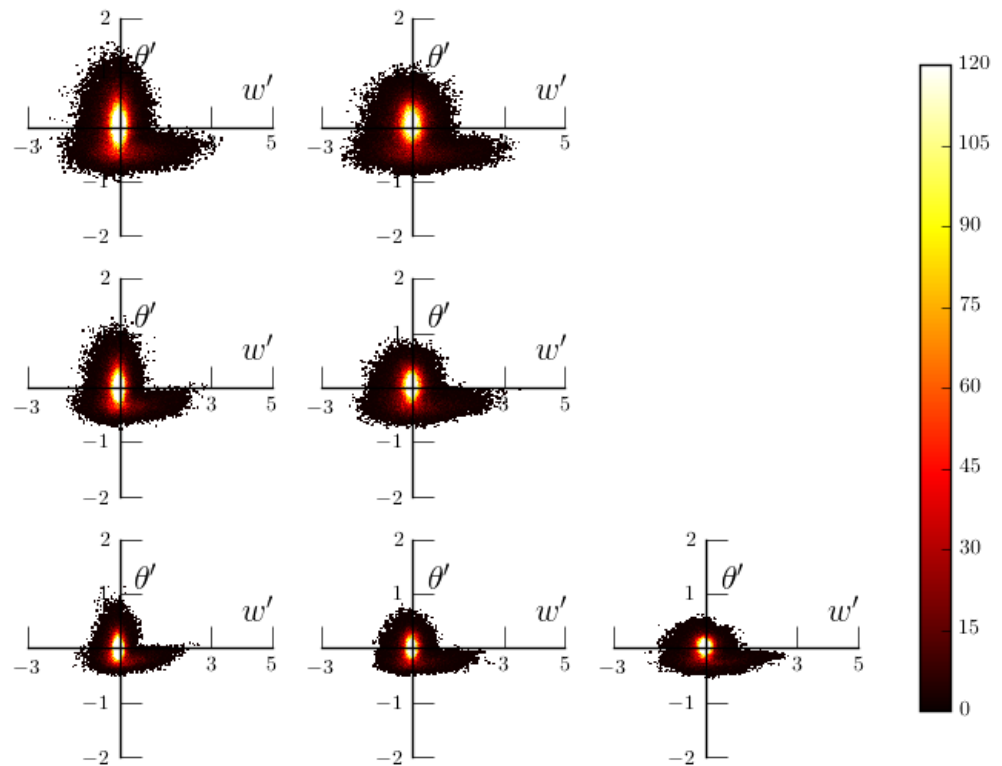
**Figure 4.3:** Histograms of local ML heights ( $h_0^l$ ) are shown in (a), (b) and (c). Probability distributions of scaled local ML height ( $\frac{h_0^l}{h}$ ) are shown in (d), (e) and (f). Both sets of plots are taken at 5 hours and darker shading represents higher  $w'\theta'_s$ . Stability decreases from top to bottom i.e (a) and (d) represents runs with the highest stability ( $\gamma = 10 \text{ Kkm}^{-1}$ ).

### 4.1.2 Local turbulent Velocity and Potential Temperature Fluctuations

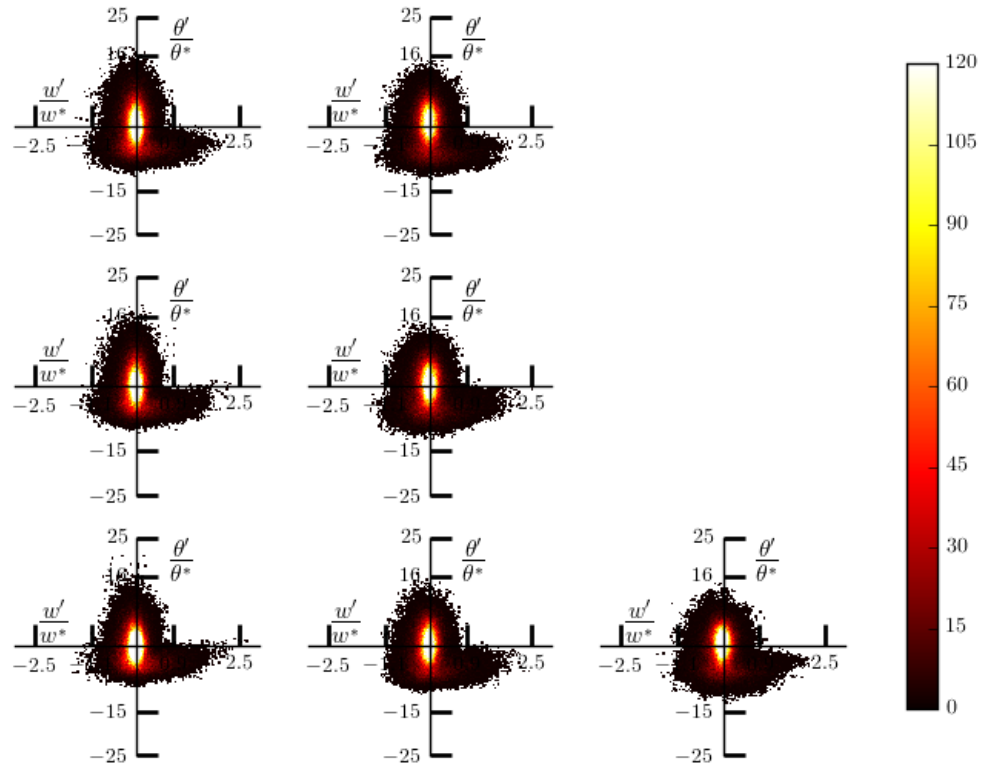
The two-dimensional histograms of  $\theta'$  and  $w'$ , at each horizontal point in each ensemble case, for all runs at  $h$  are plotted in Figure 4.4 to visualize how the distributions are influenced by changes in  $(\overline{w'\theta'})_s$  and  $\gamma$ . In order to isolate the effects of  $\gamma$ ,  $w'$  and  $\theta'$  are scaled by the convective velocity and temperature scales ( $w^*$  and  $\theta^*$ ) respectively and plotted in Figure 4.5.

Distributions of both  $w'$  and  $\theta'$  widen with increasing  $(\overline{w'\theta'})_s$ . Whereas that of  $\theta'$  increases only slightly with increasing stability ( $\gamma$ ) in Figure 4.4. As expected,  $\gamma$  inhibits both upward and downward  $w'$ . The scaled version in Figure ?? shows damping of  $w'$  where potential temperature fluctuations are positive. This can be seen as the horizontal tick marks bounding the  $\frac{w'}{w^*}$  distribution become less obscured as  $\gamma$  increases. Concurrently, the coolest negative  $\frac{\theta'}{\theta^*}$  become less cool, and the warmest become warmer. So the  $\frac{\theta'}{\theta^*}$  distribution shifts positively with increasing  $\gamma$ .

Although the quadrant of overall largest magnitude is that of upward moving cool air ( $w'^+\theta'^-$ ), in the EZ the net heat flux is downward moving warm ( $w'^-\theta'^+$ ) air as the other three quadrants approximately cancel. This is in line with the findings of Sullivan et al. (1998).



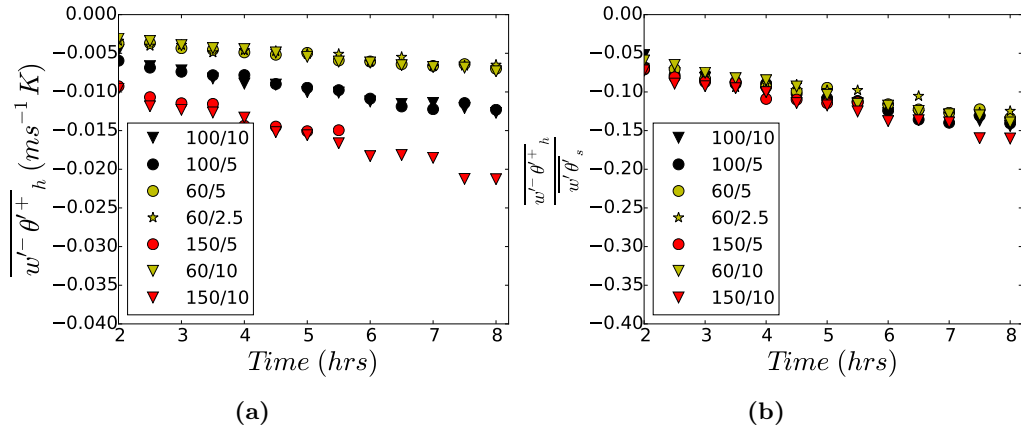
**Figure 4.4:** 2 dimensional histograms of  $w'$  and  $\theta'$  at  $h$  for  $w'\theta' = 150 - 60$  ( $Wm^{-2}$ ) (top - bottom) and  $\gamma = 10 - 2.5$  ( $Kkm^{-1}$ ) (left - right) at 5 hours



**Figure 4.5:** Two-dimensional distributions of  $\frac{w'}{w^*}$  and  $\frac{\theta'}{\theta^*}$  at  $h$  for  $(\overline{w'\theta'})_s = 150 - 60(Wm^{-2})$  (top - bottom) and  $\gamma = 10 - 2.5(Kkm^{-1})$  (left - right) at 5 hours. Tick-marks are thickened to show the narrowing of the  $\frac{w'}{w^*}$  distribution where  $\frac{\theta'}{\theta^*}$  is positive, as well as the positive shift in  $\frac{\theta'}{\theta^*}$ , as  $\gamma$  increases.

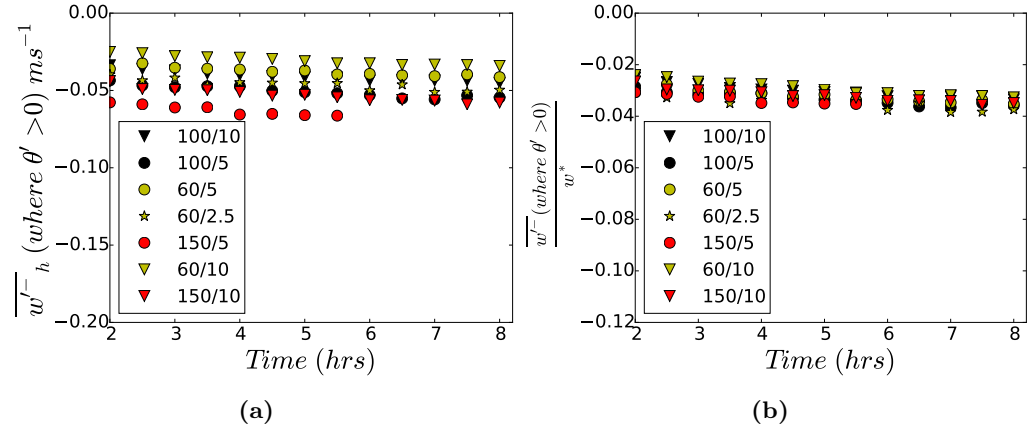
#### 4.1.3 Downward Moving Warm Air at $h$

The average downward moving warm quadrant ( $\overline{w' - \theta'}^+$ ) at  $h$  represents the pockets of trapped or engulfed warm air that become mixed into the growing CBL. So its magnitude can be taken as a measure of entrainment. Figure 4.6 shows that this increases in time, as well as with increasing  $(\overline{w' \theta'})_s$ . Grouping according to  $(\overline{w' \theta'})_s$  is evident and there is further collapse when this is applied as scale in Figure 4.6 (b). Further partitioning  $(\overline{w' - \theta'}^+)_h$  into its velocity and temperature components reveals additional complexity.



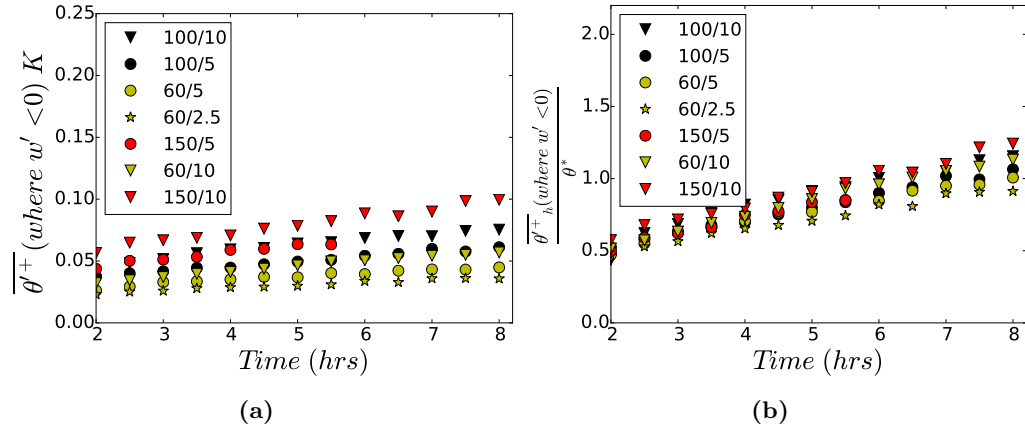
**Figure 4.6:** Plots of (a) the average downward moving warm air at  $h$  ( $\overline{w' - \theta'}^+_h$ ) and (b) ( $\overline{w' - \theta'}^+_h$ ) scaled by the average vertical turbulent heat flux ( $\overline{w' \theta'}_s$ ) vs time

Figure 4.7 shows that the velocity component  $\overline{w'^-}_h$  where  $\theta'_h > 0$ , is effectively scaled by  $w^*$ .



**Figure 4.7:** (a) Average negative vertical turbulent velocity perturbation at  $h \overline{w'^-}_h$  at points where  $\theta' > 0$  and (b)  $\overline{w'^-}_h$  where  $\theta' > 0$  scaled by  $w^*$ .

The curves representing  $\overline{\theta'^+}_h$  where  $w'_h > 0$  vs time do collapse when scaled by  $\theta^*$  in Figure 4.8. However, Figure 4.9 shows this component approaching a constant proportion of the potential temperature scale introduced in Section 1.2.6,  $\delta h \gamma$ , thus indicating that the effects of  $\gamma$  on the positive potential temperature fluctuations at  $h$  are more important than  $(\overline{w' \theta'})_s$ .



**Figure 4.8:** (a) Average positive potential temperature perturbation  $\overline{\theta'^+}_h$  at points where  $w' < 0$  and (b)  $\overline{\theta'^+}_h$  where  $w' < 0$  scaled by  $\theta^*$ .

#### 4.1.4 Answer to Q1 Entrainment Zone Structure

Using a multi-linear regression method, the local ML heights ( $h_0^l$ ) were determined. Although at each horizontal point an ML of almost uniform  $\theta$  based on the local profiles is evident, the region directly above it differs depending on location as well as from the average profile. Since there is no reliable, local definition of  $h$ , I take the distributions of local ML height ( $h_0^l$ ) to be a measure of CBL height variance in space and so the EZ. These distributions approached similarity when scaled by  $h$ , showing an increase in the lower boundary (or percentile) with increased  $\gamma$ . I interpret this result as an indication that increased  $\gamma$  results in a narrower scaled EZ depth.

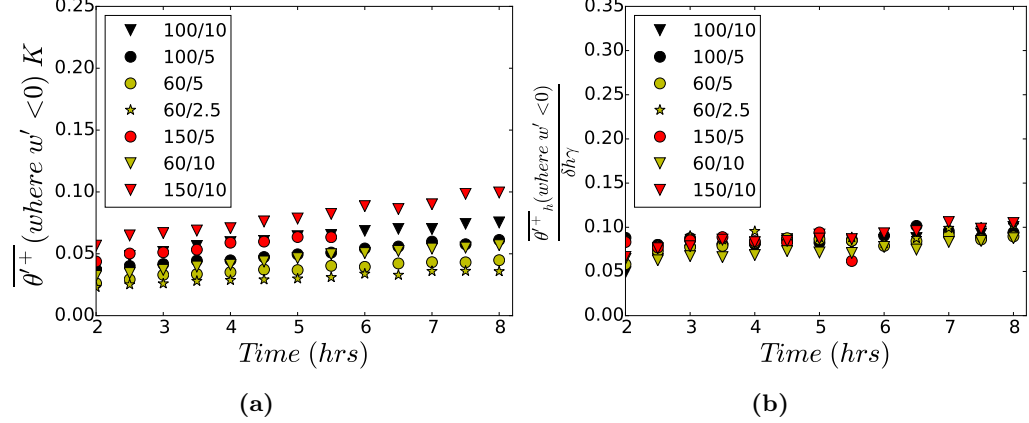


**Figure 4.9:** (a) Average positive potential temperature perturbation at  $h \theta_h'^+$  at points where  $w' < 0$  and (b)  $\overline{\theta'^+}_h$  where  $w' < 0$  scaled by  $\gamma \Delta h$ .

Two dimensional distributions of the local turbulent fluctuations,  $w'$  and  $\theta'$  at  $h$  show some variation with  $\gamma$  when scaled by the convective scales  $w^*$  and  $\theta^*$ . The distribution of  $\frac{w'}{w^*}$  where  $\frac{\theta'}{\theta^*}$  is positive narrows, while  $\frac{\theta'}{\theta^*}$  shifts positively.

Plots of the average downward moving warm quadrant at  $h$  ( $(\overline{w'}\overline{\theta'})_h$ ) show dependence on  $(\overline{w'}\overline{\theta'})_s$ . Breaking  $(\overline{w'}\overline{\theta'})_h$  into its two components reveals dependence on both  $(\overline{w'}\overline{\theta'})_s$  and  $\gamma$ . The average downward moving velocity at  $h$  ( $(\overline{w'})_h$ ), at points where there is a positive potential temperature perturbation ( $\theta'^+$ ), show clear dependence on  $w^*$ . Whereas the average positive potential temperature perturbation  $\overline{\theta'^+}_h$  where  $w'$  is negative seems to approach a constant value of  $\delta h \gamma$ . So as one would expect, the potential temperature of the entrained warm air depends on  $\gamma$ .

## 4.2 Q2 Entrainment Zone Boundaries

### 4.2.1 EZ Boundaries based on the average vertical Potential Temperature Gradient Profiles

In Figure 4.10 (a) the scaled upper EZ boundaries collapse to an initial value of approximately 1.15, decreasing to about 1.1. The scaled lower EZ boundaries appear grouped according to  $\gamma$  and increase with respect to time. So overall the scaled EZ ( $\frac{h_1}{h}$  -  $\frac{h_0}{h}$ ) narrows with time.

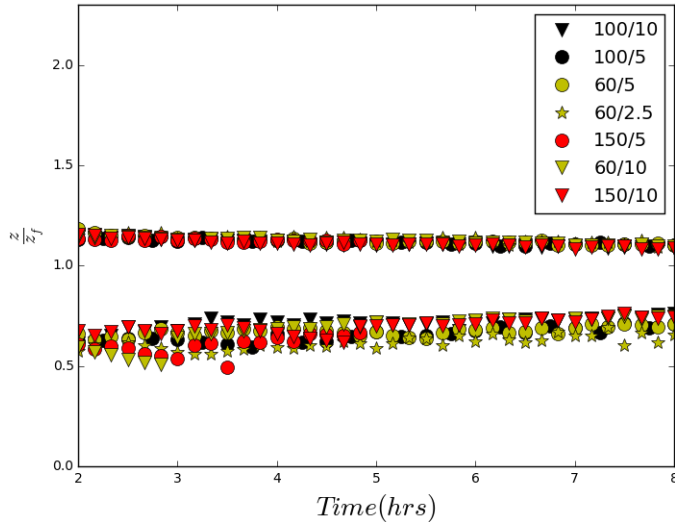


**Figure 4.10:** Plot of scaled EZ upper ( $\frac{h_1}{h}$ ) and lower ( $\frac{h_0}{h}$ ) boundaries based on the average vertical potential temperature gradient profile.

The lower entrainment zone boundary  $h_0$ , as illustrated in Figure 4.11 is the point at which the vertical  $\frac{\partial \bar{\theta}}{\partial z}$  profile exceeds a threshold ( $.0002Kkm^{-1}$ ), chosen such that it is positive and at least an order of magnitude smaller than  $\gamma$ . As suggested by the results of Section 4.1.1, the scaled EZ depth decreases with increasing Richardson number ( $Ri = \frac{\frac{g}{\bar{\theta}_{ML}} \Delta \theta h}{w^*{}^2}$ ) as in Table

4.1). However, grouping of the curves representing

$$\frac{\Delta h}{h} \propto Ri^b \quad (1.15)$$

according to  $\gamma$  is evident in Figure 4.12.

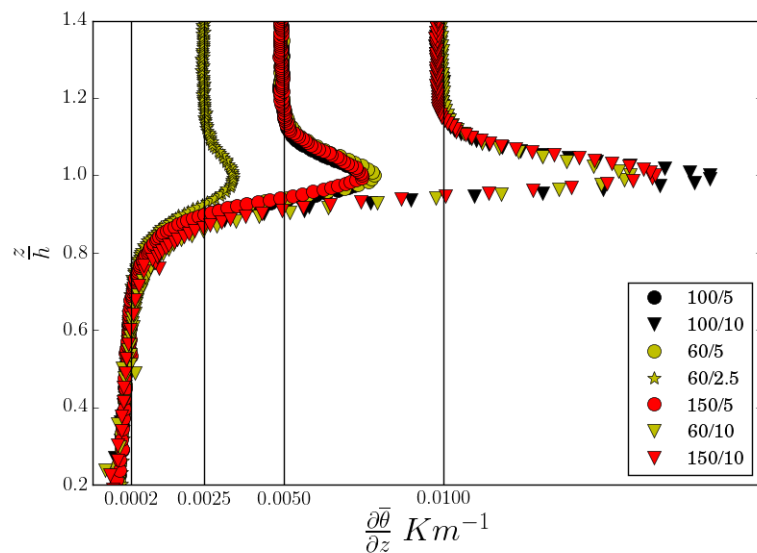


**Figure 4.11:**  $\frac{\partial \bar{\theta}}{\partial z}$  profiles with threshold at  $.0002 Kkm^{-1}$

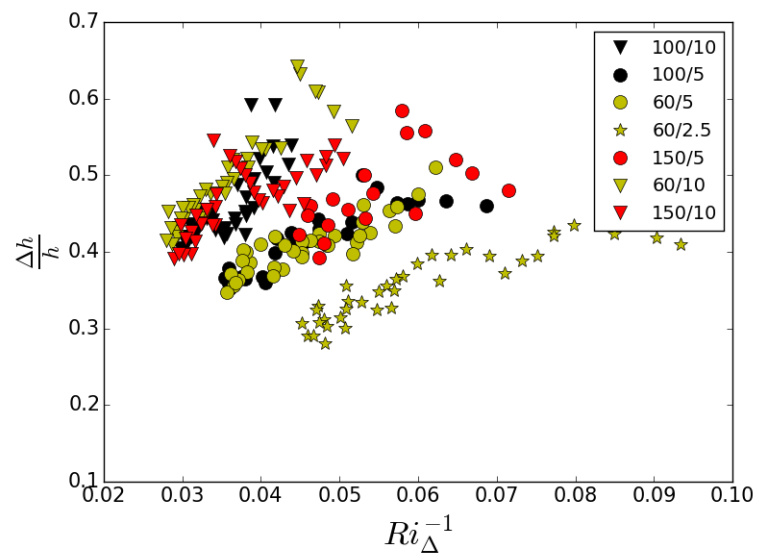


**Figure 4.12:** Scaled EZ depth ( $\frac{h_1 - h_0}{h}$ ) vs inverse Richardson number ( $Ri_{\Delta}^{-1}$ ) with threshold at  $.0002Kkm^{-1}$

### Threshold Test for lower EZ Boundary, $h_0$

To explore how varying the threshold value effects Equation 1.15, plots analogous to Figure 4.12 were produced at two additional thresholds. In Figure 4.13, a higher value ( $.0004Kkm^{-1}$ ) results in a higher  $h_0$  and so a narrower EZ. In Figure 4.14, a lower threshold value ( $.0001Kkm^{-1}$ ) results in a lower  $h_0$ . Both of these threshold values result in grouping according to  $\gamma$ .

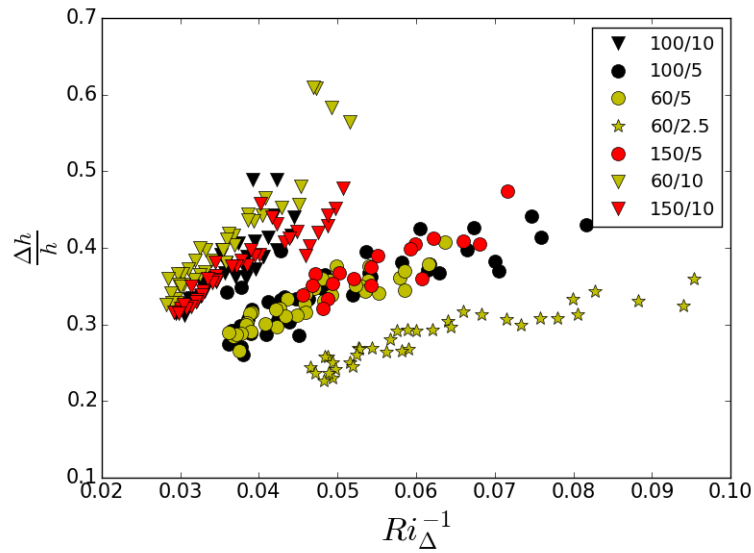


**Figure 4.13:** Scaled EZ depth vs inverse Richardson Number with threshold at  $.0004Kkm^{-1}$

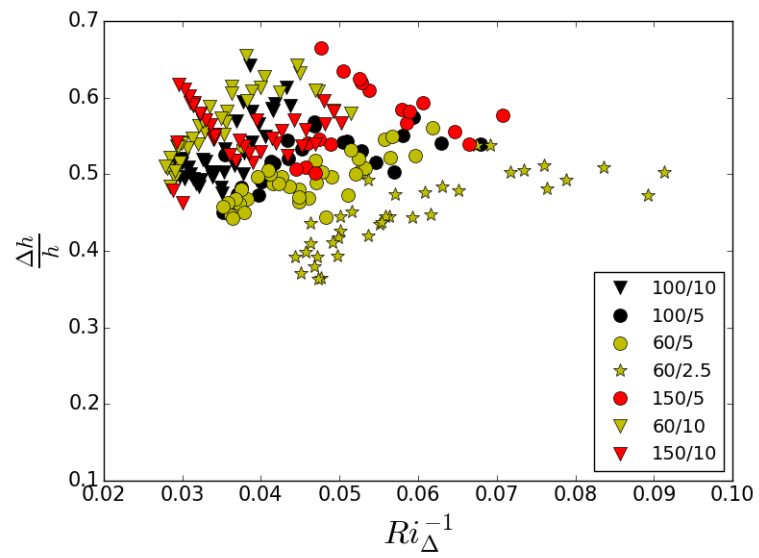


**Figure 4.14:** Scaled EZ depth vs inverse Richardson number ( $Ri^{-1}$ ) with threshold at  $.0001Kkm^{-1}$

#### 4.2.2 EZ Boundaries based on scaled vertical Potential Temperature Gradient Profiles

The curves representing Equation 1.15

$$\frac{\Delta h}{h} \propto Ri^b \quad (1.15)$$

collapse when the heights are defined based on the scaled vertical potential temperature gradient ( $\frac{\partial \bar{\theta}}{\partial z}$ ) profile in Figure 4.19. This stems from a switch in the relative magnitudes of the vertical potential temperature gradient in the upper ML which can be seen when Figure 4.15 is compared to Figure 4.11. So from here on all heights will be defined based on the scaled average profiles.

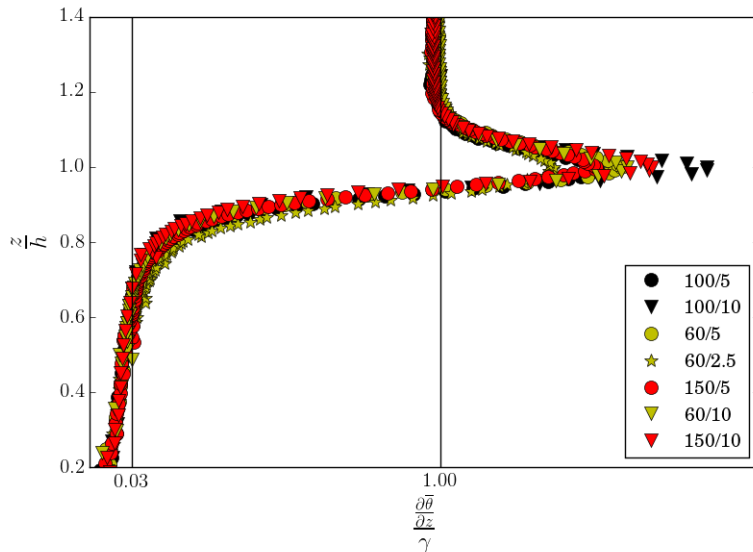


**Figure 4.15:** Scaled  $\frac{\partial \bar{\theta}}{\partial z}$  profiles with threshold at .03

Figure 4.17 supports an exponent  $b = -\frac{1}{2}$  at lower values of  $Ri$ , increasing to  $b = -1$  at higher  $Ri$ .

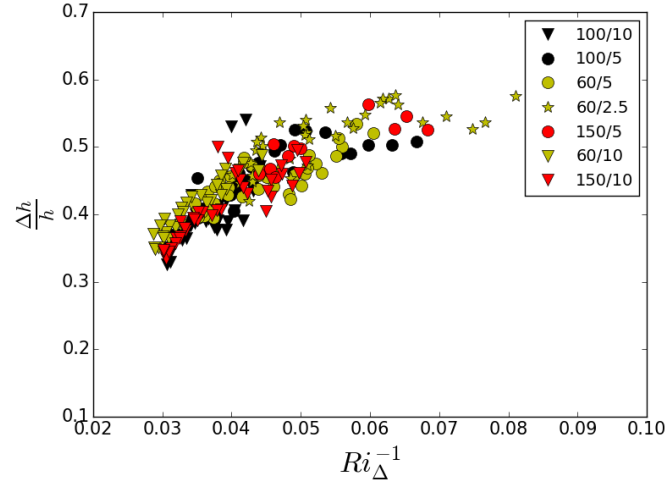


**Figure 4.16:** Plots of scaled EZ depth vs  $Ri^{-1}$ . EZ boundaries and so  $\Delta\theta$  are based on the  $\frac{\overline{w'\theta'}}{(w'\theta')_s}$  profile.

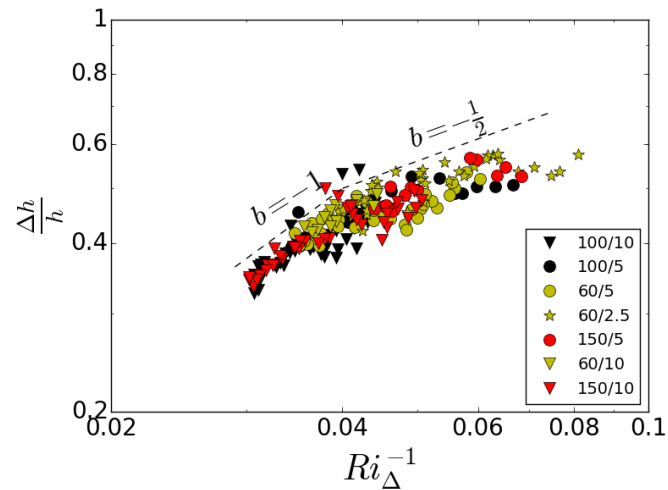


**Figure 4.17:** Scaled EZ depth vs  $Ri^{-1}$  based on the  $\frac{\partial \bar{\theta}}{\gamma \partial z}$  profile in log-log coordinates to see likely values of the exponent  $b$

#### 4.2.3 EZ Boundaries based on scaled Heat Flux Profiles

When based on the vertical heat flux profile, the scaled EZ depth ( $\frac{z_{f0}-z_{f1}}{z_f}$ ) remains more less constant with respect to time in Figure 4.18. Figure 4.19 shows little or no  $Ri$  dependence.

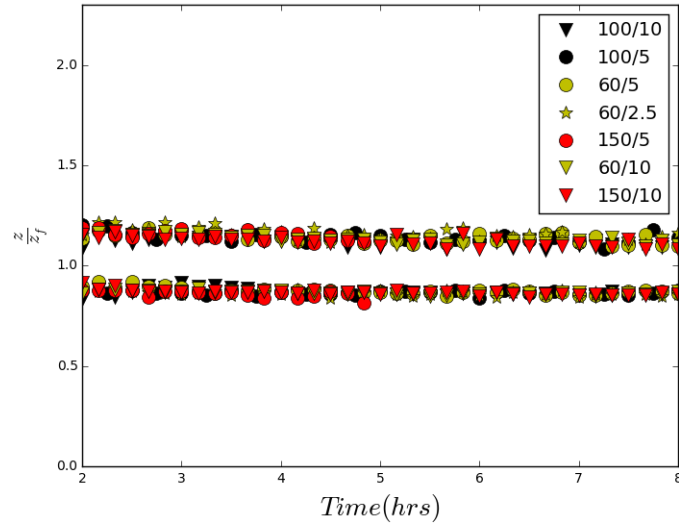


**Figure 4.18:** Plot of scaled upper ( $\frac{z_{f1}}{z_f}$ ) and lower ( $\frac{z_{f0}}{z_f}$ ) EZ boundaries based on vertical heat flux profile

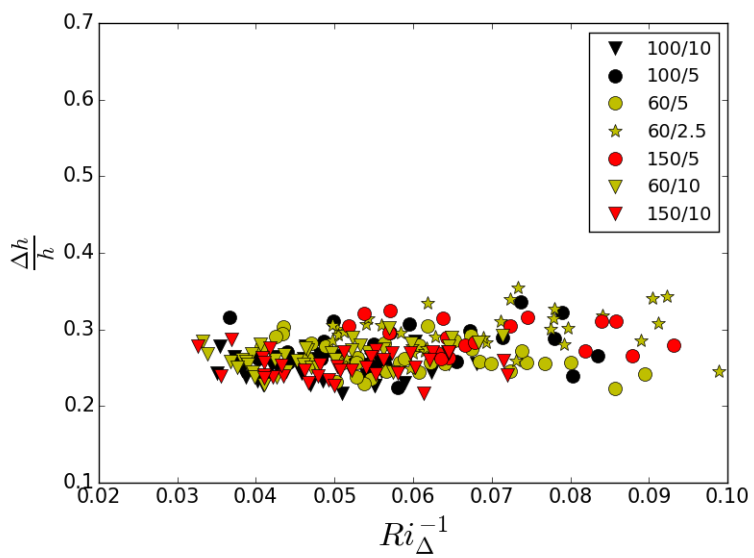


**Figure 4.19:** Plots of scaled EZ depth vs  $Ri_{\Delta}^{-1}$ . EZ boundaries and so  $\Delta\theta$  are based on the  $\frac{\overline{w'\theta'}}{(w'\theta')_s}$  profile.

#### 4.2.4 Answer to Q2 Entrainment Zone Boundaries

Initially, the CBL height and EZ boundaries are defined based on the vertical  $\frac{\partial \bar{\theta}}{\partial z}$  profile. As Brooks and Fowler (2012) point out, when using an average vertical tracer profile there is no universal criterion for a significant gradient. So a threshold value for the lower EZ boundary ( $h_0$ ) was chosen such that it was positive, small i.e. an order of magnitude less than  $\gamma$  and the same for all runs. For the sake of rigor, plots of the relationship

$$\frac{\Delta h}{h} \propto Ri^b \quad (1.15)$$

were produced based on two additional threshold values yielding analogous results. In all three cases curves representing Equation 1.15 grouped according to  $\gamma$

The importance of  $\gamma$  is revealed again as the curves representing equation 1.15 become similar when heights are based on the scaled  $\frac{\partial \bar{\theta}}{\partial z}$  profile,  $\frac{\partial \bar{\theta}}{\partial z} / \gamma$ . Further inspection shows that this change primarily occurs at the lower EZ boundary ( $h_0$ ) when  $\frac{\partial \bar{\theta}}{\partial z}$  is measured as proportion of  $\gamma$ . The influence of  $\gamma$  on  $\frac{\partial \bar{\theta}}{\partial z}$  at  $h_0$  ties in with the influence of  $\gamma$  on downward moving  $\theta'^+$  at  $h$  shown in Section 4.1.3. This prompts the use of the scaled profiles for the heights ( $h_0$ ,  $h$ ,  $h_1$  and  $z_{f0}$ ,  $z_f$ ,  $z_{f1}$ ) in the subsequent section.

These results support a varying exponent  $b$  in Equation 1.15 which is lower in magnitude ( $-\frac{1}{2}$ ) at lower  $Ri$  and approaches  $-1$  at higher  $Ri$ . For comparison with results from other studies these heights are also based on the vertical  $\overline{w' \theta'}$  profiles as shown in Figure 1.6. I find no clear dependence of the scaled EZ depth on  $Ri$  within this framework.

## 4.3 Q3 Entrainment Rate Parameterization

### 4.3.1 Reminder of Definitions

A key finding of Section 4.2.2 was that curves representing Equation 1.15 group according to  $\gamma$  when heights are based on the unscaled  $\frac{\partial \bar{\theta}}{\partial z}$  profile and then become similar when heights are based on  $\frac{\partial \bar{\theta}}{\gamma}$ . So from here on all heights will be as in Figure 4.20 and the corresponding Richardson numbers ( $Ri$ ) will be as in Table 4.1.

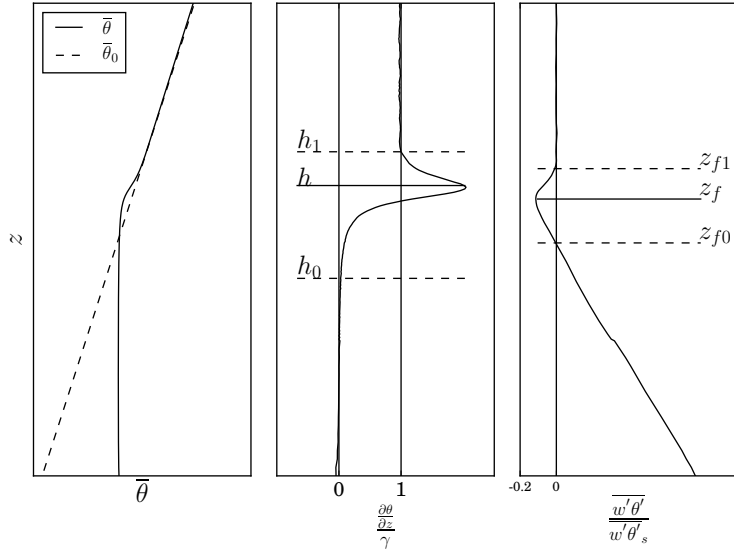


**Figure 4.20:** Height definitions based on the scaled average vertical profiles.  $\theta_0$  is the initial potential temperature.

### 4.3.2 CBL Growth

Convective boundary layer height ( $h$ ) in Figure 4.21 increases, rapidly at first, with a steadily decreasing rate and relates to the square-root of time in Figure 4.22. Federovich et al. (2004) focus on the attainment of a quasi-steady state regime in which their zero-order model applies. Within this

**Table 4.1:** Definitions based on the vertical  $\bar{\theta}$  profile in Figure 1.6. To obtain those based on the  $w'\theta'$  profile, replace  $h_0$ ,  $h$  and  $h_0$  with  $z_{f0}$ ,  $z_f$  and  $z_{f1}$

CBL Height	ML $\bar{\theta}$	$\theta$ Jump	Ri
$h$	$\bar{\theta}_{ML} = \frac{1}{h} \int_0^h \bar{\theta}(z) dz$	$\Delta\theta = \bar{\theta}(h_1) - \bar{\theta}(h_0)$	$Ri_\Delta = \frac{\frac{g}{\bar{\theta}_{ML}} \Delta\theta h}{w^{*2}}$
		$\delta\theta = \bar{\theta}_0(h) - \bar{\theta}_{ML}$	$Ri_\delta = \frac{\frac{g}{\bar{\theta}_{ML}} \delta\theta h}{w^{*2}}$

regime scaled CBL height ,  $hB_s^{-\frac{1}{2}}N^{\frac{3}{2}}$  where  $B_s$  is the surface buoyancy flux, relates to the square-root of their scaled time,  $tN$ . Over the time of the runs  $B_s$  is constant and  $N$  varies much more slowly than  $h$ . So based on Figure 4.22 I conclude that over the period during which I obtain output, all runs are in this quasi-steady state. The height of minimum vertical heat flux  $z_f$  is a constant proportion of  $h$  in Figure 4.23 indicating that this point advances more slowly than  $h$ .

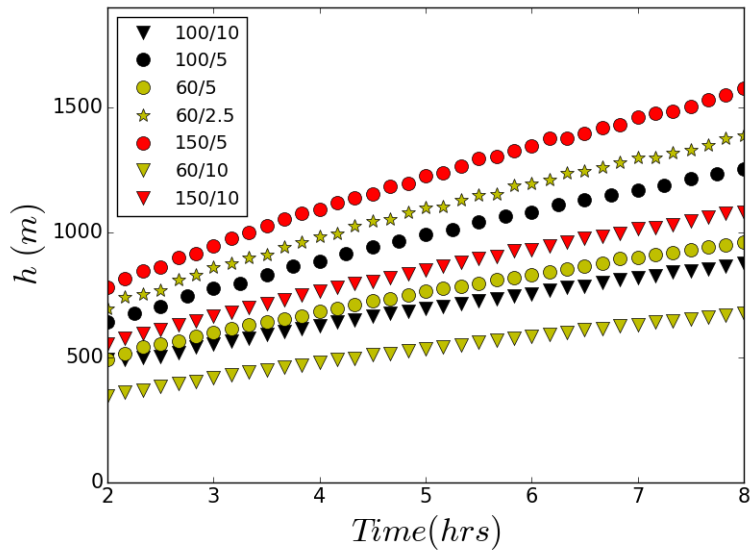


**Figure 4.21:**  $h$  vs time for all runs

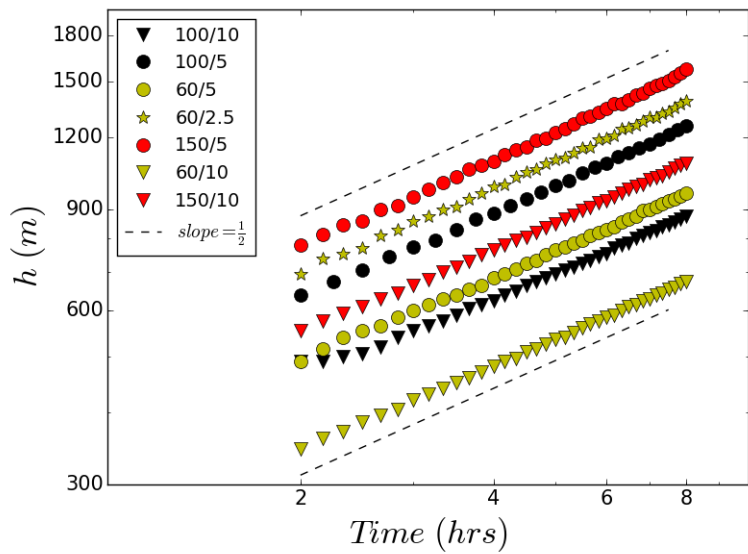


**Figure 4.22:**  $h$  vs time for all runs on log-log coordinates

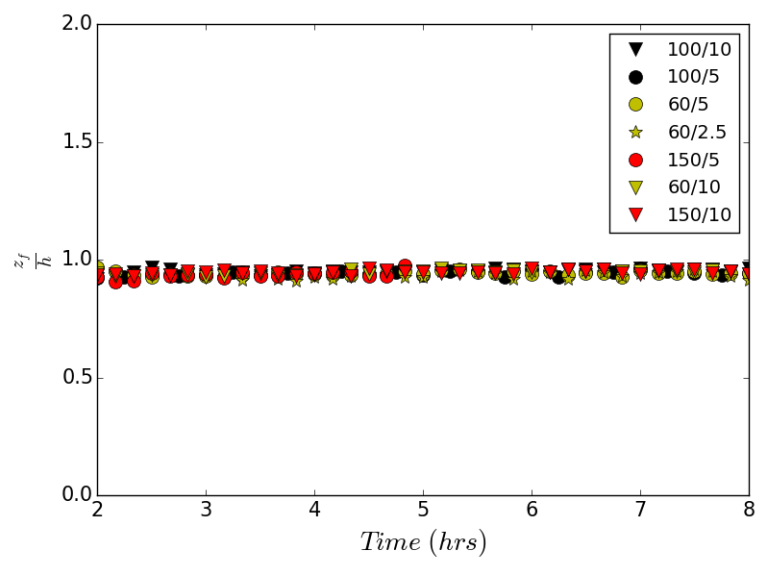


**Figure 4.23:**  $\frac{z_f}{h}$  vs Time

### 4.3.3 Heights based on the scaled vertical average Potential Temperature Profile

The inverse Richardson numbers ( $Ri_{\Delta}^{-1}$  and  $Ri_{\delta}^{-1}$ ) in Figure 4.24 decrease in time and group according to  $\gamma$ . There is an overall difference in magnitude since  $\Delta\theta > \delta\theta$ .

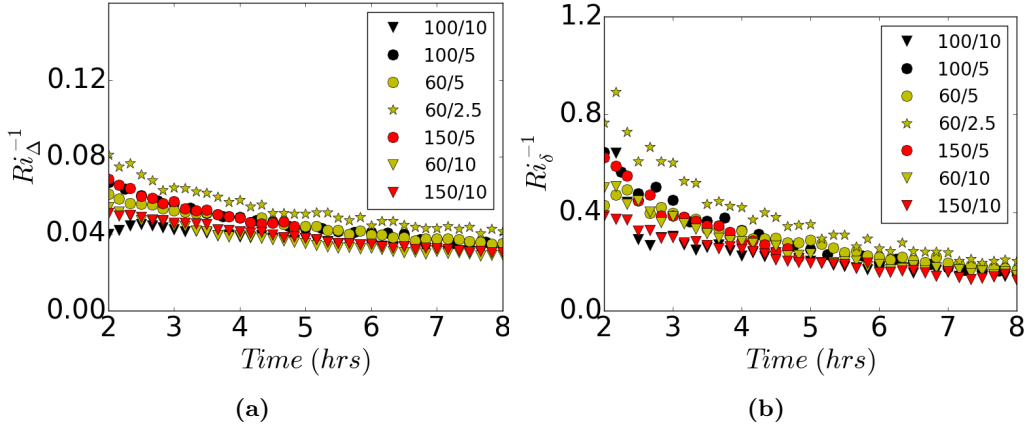


**Figure 4.24:** Inverse Richardson number vs time based on the  $\frac{\partial \bar{\theta}}{\gamma \partial z}$  profile using  $\Delta\theta$  across the EZ in (a) and  $\delta\theta$  at  $h$  in (b). See Table 4.1.

The entrainment rate ( $w_e = \frac{dh}{dt}$ ) is determined from the slope of a second order polynomial fit to  $h(\text{time})$  in Figure 4.21. When  $w_e$  is scaled by  $w^*$ , the resulting relationship to  $\text{Ri}_\Delta$ , plotted in log-log coordinates in Figure 4.25 (a),

$$\frac{w_e}{w^*} \propto \text{Ri}_\Delta^a \quad (4.1)$$

has an exponent  $a = -1$  at lower  $\text{Ri}_\Delta$  and  $a = -\frac{3}{2}$  at higher  $\text{Ri}_\Delta$ .

In Figure 4.25 (b) the relationship

$$\frac{w_e}{w^*} \propto \text{Ri}_\delta^a \quad (4.2)$$

possibly approaches a value of  $a = -1$  at higher  $\text{Ri}_\delta$  but a value of lower in magnitude would fit better overall.

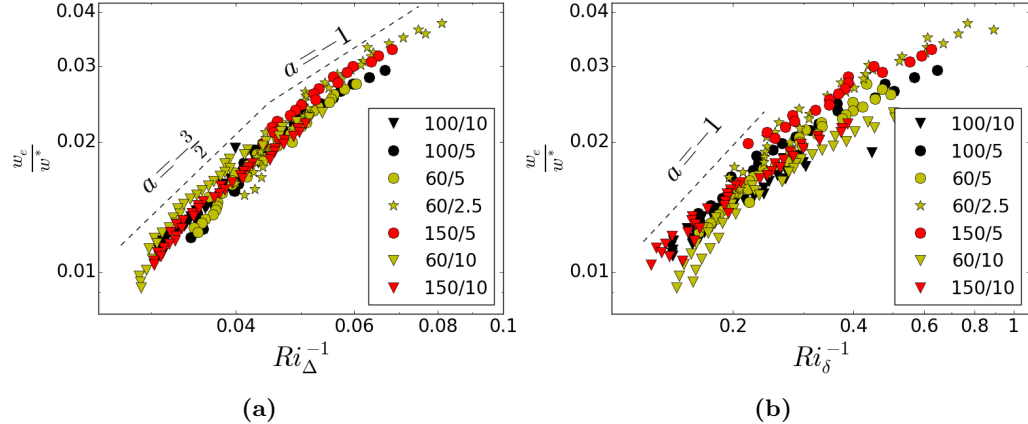


**Figure 4.25:** Scaled entrainment rate vs inverse Richardson number ( $\text{Ri}^{-1}$ ), in log-log coordinates, where  $\text{Ri}$  is based on the  $\frac{\partial \bar{\theta}}{\gamma}$  profile using  $\Delta\theta$  across the EZ in (a) and  $\delta\theta$  at  $h$  in (b). See Figure 4.20.

#### 4.3.4 Heights based on the scaled vertical average Heat Flux Profile

Richardson numbers with  $\Delta\theta$  and  $\delta\theta$  based on the  $\bar{w}'\theta'$  profile are comparable with those in Section 4.3.3 although  $Ri_\Delta$  shows considerable scatter in Figure 4.26 (a).

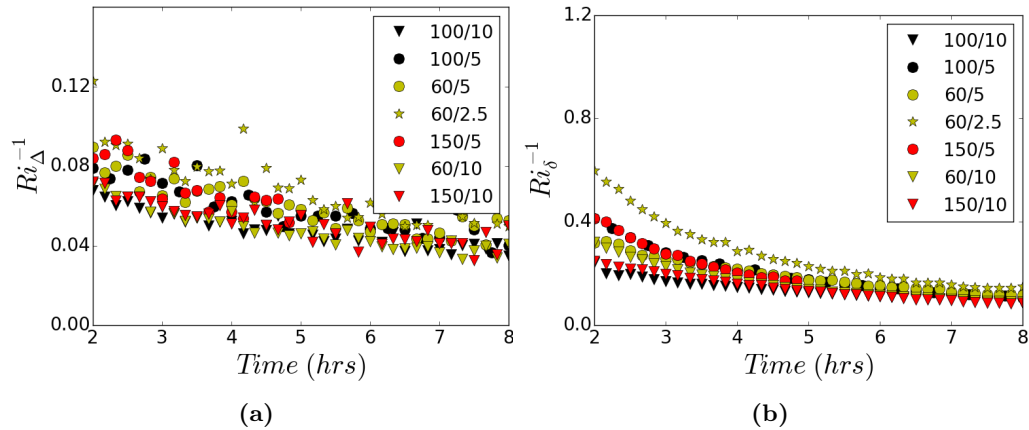


**Figure 4.26:** Inverse Richardson number vs time based on the  $\frac{\overline{w' \theta'}}{w' \theta'_s}$  profile using  $\Delta\theta$  across the EZ in (a) and  $\delta\theta$  at  $z_f$  in (b). See Figure 1.6.

In Figure 4.27 the axes are in log-log coordinates and all heights are based on the scaled  $\overline{w'\theta'}$  profile. The relationship of scaled entrainment rate to  $Ri_\Delta$  in (a) shows scatter and either value of  $a$  or a value in between could fit. Whereas the exponent in the relationship to  $Ri_\delta$  in (b) seems to change throughout the run(s) and a value less (in magnitude) than  $-1$  might fit better.

#### 4.3.5 Answer to Q3 Entrainment Rate Parameterization

In conclusion the relationship of scaled entrainment rate to  $Ri_\Delta$  based on the  $\frac{\partial \bar{\theta}}{\partial z}$  profile shows the least scatter over time and between runs in Figure 4.25. Here the exponent seems to start at a value close to  $-1$  increasing, with higher  $Ri$ , to close to  $-\frac{3}{2}$ . This apparent change with increased  $Ri$

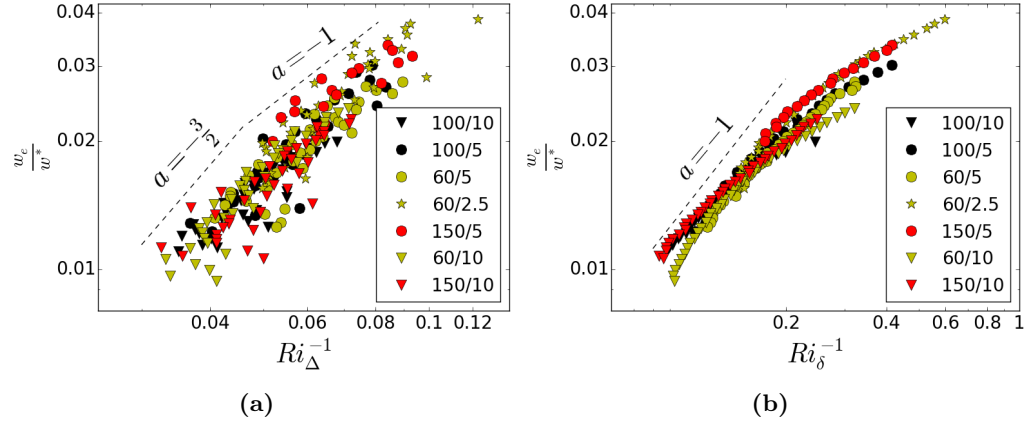


**Figure 4.27:** Scaled entrainment rate vs inverse Richardson number ( $Ri^{-1}$ ), in log-log coordinates, where  $Ri$  is based on the  $\frac{\overline{w'\theta'}}{(w'\theta')_s}$  profile using  $\Delta h$  across the EZ in (a) and  $\delta\theta$  at  $z_f$  in (b). See Figure 1.6.

mirrors that seen with Equation 1.15 in Figure 4.17. It's possible that it represents a change in entrainment mechanism as discussed in Section 1.2.6. Overall the definition of the temperature jump certainly has an effect,  $\Delta\theta$  yielding a higher value of  $a$  than  $\delta\theta$ .

## 5. Results in Context

Much work has been done to develop our understanding of CBL entrainment, so this chapter will focus on how my results fit into the discussion established in the literature. I hone in on five closely related publications for comparison. Sullivan et al.'s 1998 LES study was seminal in shedding light on CBL entrainment zone structure. Whereas Brooks and Fowler's (2012) work contains the most recent LES results on the topic framed within an up to date review of CBL height and EZ definitions. Federovich et al. (2004) bridges LES and bulk models, while the closely related DNS study of Garcia and Mellado (2014) introduces the two-layer EZ concept and answers questions regarding the scale resolution required to realistically capture CBL growth and EZ structure. Sullivan and Patton (2011) addressed this last point using an LES, and was pivotal in guiding the choice of grid-size in the study described in this thesis. Finally Sorbjan (1996) focused on the effects of upper lapse rate on the turbulence in the upper CBL and provided ideas upon which I based Section 4.1.

Section 5.1 draws upon the results of Sullivan and Patton (2011) to address the need for high resolution in the entrainment zone (EZ) such that the steep gradients are sufficiently represented. I present and compare those of my results that are pertinent and refer to how Garcia and Mellado (2014) speaks to this point. Finally, I touch upon how my domain size and initial conditions compare with those of the similar LES studies the bearing in mind possible implications of the similarities and differences.

In Section 5.2 I describe problems encountered when using the gradient

method, as well as discuss the results obtained using my chosen method of determining local ML height. All of this is set in context with the results of Sullivan et al.'s 1998 and Brooks and Fowler's (2012). The influence of  $\gamma$  on the turbulent fluctuations of vertical velocity and potential temperature is discussed and compared with the results of Sorbjan (1996) before addressing the dependence of the downward moving positive potential temperature fluctuations at  $h$  on this parameter. An explanation of the potential temperature fluctuation scale  $\delta h\gamma$  follows.

A primary goal of this thesis was to test the average  $\theta$  profile as a basis for defining the EZ boundaries. Before comparing the results using heights thus defined in Section 5.3, I base all heights on the vertical heat flux ( $\overline{w'\theta'}$ ) profile to enable direct comparison with the results of Brooks and Fowler (2012) and Federovich et al. (2004). I discuss similarities, differences and possible reasons for the latter. I then compare results based on the potential temperature profile focusing on the exponent  $b$  in Equation 1.15 and how it varies depending on  $Ri$ .

Section 5.4 contains an analogous comparison to that described above. Heights are defined, first based on the vertical heat flux profile for direct comparison with the results of Federovich et al. (2004) and Garcia and Mellado (2014) and then based on the average  $\theta$  profile. Each of these two comparisons is further broken into two, in order to address the effect of, defining the  $\theta$  jump across the EZ as in Figure 1.3, vs at  $h$  as in Figure 1.4. In all, there are four plots of Equation 1.24 for the purpose of observing how the exponent  $a$  varies depending on  $\theta$  jump definition, as well as with  $Ri$ . This variation is discussed in the context of the results of the other comparable studies.

## 5.1 Comparison of general Set-up

### 5.1.1 Significance of Grid-size

Sullivan and Patton (2011) found that the shapes of the average potential temperature ( $\bar{\theta}$ ) and heat flux ( $\overline{w'\theta'}$ ) profiles, as well as the measured CBL height vary depending on grid size. The resolution at which convergence begins is listed in Table 5.1. At lower resolution the  $\bar{\theta}$  and  $\overline{w'\theta'}$  profiles are such that the entrainment zone (EZ) is a larger portion of the CBL and measured CBL height is higher. Overall they concluded that vertical resolution was critical. This compliments the conclusion Brooks and Fowler (2012) reached when discussing their resolution test. That is, to capture the steep vertical gradients in the EZ requires high vertical resolution.

**Table 5.1:** Grid spacing around the EL used in comparable LES studies. Those used for resolution tests are not listed here. For Sullivan and Patton's 2011 resolution study I list the grid sizes at which profiles within the EL and CBL height evolution began to converge.

Publication	$\Delta x, \Delta y, \Delta z$ in the EZ (m)	Horizontal Domain ( $\text{km}^2$ )
Publication		
Sullivan et al. (1998)	33, 33, 10	5 x 5
Federovich et al. (2004)	100, 100, 20	5 x 5
Brooks and Fowler (2012)	50, 50, 12	5 x 5
Sullivan and Patton (2011)	20, 20, 8	5 x 5
This study	25, 25, 5	3.4 x 4.8

As Turner discusses in his 1986 review of turbulent entrainment, smaller scale processes such as those at the molecular level are relatively unimportant. Large scale engulfment and trapping between thermals dominates. If the ergodic assumption holds and potential temperature variance ( $\overline{\theta'^2}$ ) is calculated based on the difference at a point from the horizontal average, it

is a measure of horizontal variance at a point in time. Sullivan and Patton (2011) found that the vertical distance over which  $\overline{\theta'^2}$  varied significantly, more or less converged at the resolution shown in Table 5.1. But the maximum  $\overline{\theta'^2}$  continued to increase up to their finest grid spacing ( $\Delta x = 5$ ,  $Delta y = 5$ ,  $Delta z = 2$ ).

The question as to whether mixing and gradients within the EZ are adequately resolved motivates DNS studies such as that of Garcia and Mellado (2014). These authors found the entrainment ratio ( $\frac{\overline{w'\theta'}_{z_f}}{\overline{w'\theta'}_s}$ ) to be about 0.1 which is lower than observed by Federovich et al. (2004), but close to what was seen here in Figures 3.5 and 3.2. Based on their  $\overline{w'\theta'}$  profiles the depth of the region of negative flux is comparable to what is shown in Figure ???. Furthermore, these authors concluded that the production and destruction rates of turbulence kinetic energy (TKE), as well as the entrainment ratio used to calculate the entrainment rate, were effectively independent of molecular scale processes.

The FFT energy spectra of the turbulent velocities at the top of the ML show a substantial resolved inertial subrange giving confidence in the choice of horizontal grid size used. In the EZ where turbulence is intermittent, the dominant energy containing structures are smaller, and decay to the smallest resolved turbulent structures is steeper. This confirms the assertion of Garcia and Mellado (2014) that the EZ is separated into two sub-layers in terms of turbulence scales.

### 5.1.2 Horizontal Domain

The horizontal domain in this study is relatively small (see Table 5.1). However, visualizations of horizontal and vertical slices clearly showed multiple resolved thermals. Their diameters increased with CBL height, but remained less than or on the order of 100 meters. Sullivan et al. (1998) carried out one run on a smaller domain with higher resolution, noticed it resulted

in lower CBL height and concluded this was due to restricted horizontal thermal size. However, given the results of Sullivan and Patton (2011) it could have been an effect of grid-size.

When defining heights based on average profiles Sullivan et al. (1998) produced jagged, oscillating time-series and Brooks and Fowler (2012) encountered significant scatter in plots of Equation 1.24. But the heights based on average profiles here, using an ensemble of cases, varied smoothly in time. This could be attributed to a smoother profile based on a greater number horizontal points ( $10*128*192$ ).

### 5.1.3 Initial Conditions

The principle parameter describing the balance of forces in dry, idealized CBL entrainment is the Richardson number ( $Ri$ ) and its magnitude depends on the way in which the  $\theta$  jump is defined. Varying the  $\theta$  jump definition causes identical conditions to be described by different  $Ri$  values. The  $Ri$  range in this study was dependent on variation in  $\gamma$  (see Figure 4.24). Brooks and Fowler (2012) and Sullivan et al. (1998) imposed a  $\theta$  jump of varying strength topped by a constant  $\gamma$ . Whereas Federovich et al. (2004) initialized with a layer of uniform  $\theta$ . They varied  $\gamma$  and kept  $\overline{w'\theta'}$  constant for each run. Their initial conditions, definitions of the  $\theta$  jump and  $Ri$  range are directly comparable to those of this study, whereas those of Brooks and Fowler (2012) and Sullivan et al. (1998) are quite different.

## 5.2 Entrainment Zone Structure

### 5.2.1 Local ML Heights

Sullivan et al. (1998) determined local CBL height by locating the point of maximum  $\theta$  gradient. Analysis of the resulting distributions showed dependence of standard deviation and skewness on Richardson number ( $Ri$ ). The

**Table 5.2:** Initial conditions used in comparable LES studies.

Publication	$\overline{w'\theta'_s}$ $Wm^{-2}$	$\gamma$ $Kkm^{-1}$	Initial $\theta$ Jump K	$Ri$ range
Sullivan et al. (1998)	20 - 450	3	.436 - 5.17	1 - 100
Federovich et al. (2004)	300	1 - 10	NA	10 - 40
Brooks and Fowler (2012)	10 - 100	3	1 - 10	10 - 100
This study	60 - 150	2.5 - 10	NA	10 - 30

normalized standard deviation decreased with increased  $Ri$  whereas skewness was almost bimodal; being negative at high  $Ri$  and positive and low  $Ri$ . Initially in this study, I applied a similar method and found local CBL height distributions with lower  $Ri$  to have positive skew. Upon exhaustive inspection of local vertical  $\theta$  profiles such as those in Figure 4.2, it became evident that at certain horizontal points high gradients well into the free atmosphere exceeded those closer to the location of the CBL height reasonably identified by eye.

### 5.2.2 Local ML Height Distributions

Locating the local ML height ( $h_0^l$ ) using the multi-linear regression method described in Chapter 2 proved more reliable. The resulting distributions, normalized by CBL height ( $h$ ) in Figure ??, showed a decrease in the lowest  $\frac{h_0^l}{h}$  resulting in an apparent increased negative skew with decreasing stability (decreasing  $Ri$ ). This, combined with a widening of the distribution agrees, with the findings of Sullivan et al. (1998) and supports the results based on the average profiles in Section 4.2. The approximate scaled EZ based on the  $\frac{h_0^l}{h}$  distributions is about 0.2 - 0.4 whereas that based on distributions of local maximum tracer gradients by Brooks and Fowler (2012) was smaller (.05 - .2). However, the local maximum gradient of the tracer profile would likely be within the EZ at points outside an actively impinging plume and

so higher than  $h_0^l$  defined here.

### 5.2.3 Local vertical Velocity and Potential Temperature Fluctuations

As expected, with increased  $\overline{w'\theta'_s}$  the variance and magnitude of the vertical velocity fluctuations within and at the limits of the EZ increase. Greater turbulent velocity causes a higher CBL and a deeper EZ over which: relatively warmer air from higher up is brought down; and relatively cooler air from below is brought up. So the magnitude of the potential temperature fluctuations ( $\theta'$ ) and the width of their distribution increases. All of this agrees with the findings of ? (? ), but the portion of the scaled  $w' (\frac{w'}{w^*})$  distribution where scaled  $\theta' (\frac{\theta'}{\theta^*})$  is positive, in Figure ??, appears to narrow as  $\gamma$  increases. This seems to contradict his assertion that  $w'$  is independent of this parameter while the effectiveness of  $w^*$  as a scale for  $w'^-$  where  $\theta' > 0$  in Figure 4.6 supports it.

### 5.2.4 Downward moving warm Air at $h$

Although the motion of the thermals dominates within the EZ, the  $\overline{w'^-\theta'^-}$ ,  $\overline{w'^+\theta'^-}$  and  $\overline{w'^-\theta'^+}$  quadrants do approximately cancel leaving  $\overline{w'^-\theta'^+}$  as the net dynamic, as Sullivan et al. (1998) concluded. The downward moving warm quadrant at  $h$  ( $\overline{w'^-\theta'^+}_h$ ) represents warmer free atmosphere (FA) air that is being entrained. So its magnitude, at a certain point in time, is an indication of how much the region below will be warmed due to entrainment at a successive time. The increase of  $\overline{w'^-\theta'^+}_h$  in time is primarily due to the increased average positive potential temperature fluctuation at  $h$  ( $\overline{\theta'^+}_h$ ) which is effectively scaled by the temperature scale  $(h_1 - h)\gamma = \delta h\gamma$  (see the Figures of Section 4.1.3). A similar scale was introduced by Garcia and Mellado (2014) to further their line of reasoning that the buoyancy in the upper EZ is determined by  $\gamma$ . Figure 5.1 illustrates a broad qualitative explanation. At  $h$  much of the air is at the background (or initial) potential

temperature  $\bar{\theta}_0(h)$ .

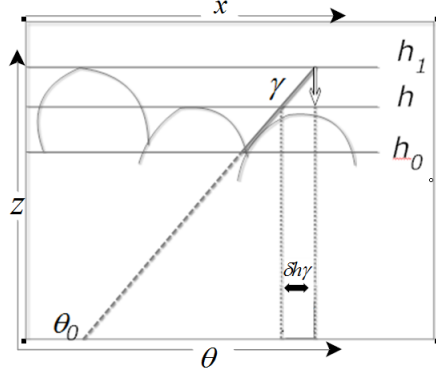


**Figure 5.1:** Illustration of the potential temperature scale  $(h_1 - h)\gamma = \delta h\gamma$ : The curves represent a vertical cross-section of thermal tops. Between them is stable air at the initial lapse rate  $\gamma$ .  $h_1$  and  $h$  correspond to the highest and average thermal height respectively and  $h_0$  is the top of the well mixed region (ML). The horizontally uniform, initial potential temperature is  $\theta_0 = \bar{\theta}_0$ . A thermal will initiate the downward movement of air from  $h_1$  to  $h$ , and the difference between its potential temperature and that of the background stable air at  $h$  is  $(h_1 - h)\gamma = \delta h\gamma$ .

Some air at potential temperature  $\theta = \bar{\theta}_0(h_1)$  is brought down from the upper EZ limit ( $h_1$ ) resulting in positive potential temperature fluctuations  $(\theta'^+)$  at  $h$ .

Garcia and Mellado (2014) suggest that the buoyancy in the lower portion of the EZ, i.e. from a point just below  $h$  down, is more strongly influenced by the vigorous turbulence of the ML than by  $\gamma$ . So mixing reduces the difference between, the potential temperature at the top of the ML, and that at or just below  $h$ . However the observation in Section 4.2.2, that the magnitude of the average vertical potential temperature gradient ( $\frac{\partial \bar{\theta}}{\partial z}$ ) in the upper ML increases with increasing  $\gamma$ , indicates that the influence of this parameter extends further down. On a related note, the magnitude of the minimum heat flux ( $\overline{w' \theta'}_{z_f}$ ) is seen to increase with increased  $\gamma$ , here and in both ? (?) and Federovich et al. (2004). It is reasonable to suggest

this leads to an increased negative vertical heat flux gradient ( $-\frac{\partial \bar{w}'\theta'}{\partial z}$ ) in the lower EZ and so increased warming per Equation 7.21.

$$\frac{\partial \bar{\theta}}{\partial t} = -\frac{\partial}{\partial z} \bar{w}'\theta' \quad (7.21)$$

### 5.3 Entrainment Zone Boundaries

The EZ is inhomogeneous, but on average is a region of transition as clearly represented by the  $\bar{\theta}$  profile. It's where relatively cooler thermals overturn or recoil initiating entrainment as represented by the vertical heat flux ( $\bar{w}'\theta'$ ) profile. The  $\bar{\theta}$  profile partially characterizes the thermodynamic state of the CBL as well defining its three layer structure. It is directly comparable to both bulk models and local  $\theta$  profiles which in turn are comparable to a sounding, unlike a  $\bar{w}'\theta'$  profile which is an inherently average quantity.

#### 5.3.1 Direct Comparison based on the vertical Heat Flux Profile

Neither of the two comparable LES studies in Table 3.3 define the EL based on the  $\frac{\partial \bar{\theta}}{\partial z}$  profile. So to enable direct comparison, heights were based on the heat flux ( $\bar{w}'\theta'$ ) profile as in Figure 4.20. In this framework Federovich et al. (2004) show decreasing scaled EZ with increasing  $Ri$  and conclude an exponent of  $b = -\frac{1}{2}$ . They attribute the decrease in the overall scaled depth to a slight decrease in the scaled upper boundary over time. However based on their plot in Figure 5.2 the decrease seems more than slight, varying from about 0.5 to 0.2.

Brooks and Fowler (2012) found no clear  $Ri$  dependence of the scaled EZ depth defined based on the  $\bar{w}'\theta'$  profile. But their definition hinged solely upon the lower part ( $z_{f1} - z_f$ ) which according to Federovich et al. (2004) does not vary in time. Figure 4.19 of this thesis shows that when I defined the EZ based on the  $\bar{w}'\theta'$  profile as Federovich et al. (2004) did, the scaled

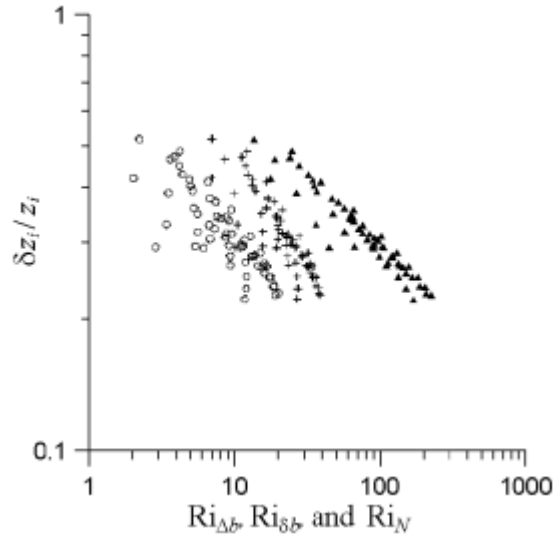


**Figure 5.2:** Figure 9 from Federovich et al. (2004) representing Equation 1.15 using three different Richardson numbers, in log-log coordinates. Heights are based on the  $\overline{w'\theta'}$  profile as in Figure 4.20 and their  $z_i$  is my  $z_f$ .  $\frac{\delta z_i}{z_i}$ .  $Ri_{\Delta b}$  (circles) and  $Ri_{\delta b}$  (crosses) correspond directly to those determined here using  $\delta\theta$  and  $\Delta\theta$ . Note that their  $\Delta$  refers to the smaller jump measured at  $z_f$ , whereas I use it for the larger.  $Ri_N$  (triangles) is the Richardson number defined in Equation 1.12, with  $w^*$  and  $z_f$  as the velocity and length scale.

EZ depth had no clear dependence on  $Ri$ . This is supported by the similarity in time and across runs of the vertical turbulent heat flux profiles when scaled by  $(\overline{w'\theta'})_s$  in Figures 3.3 and 3.5.

The most obvious possible cause for disagreement with the results of Federovich et al. (2004) is the difference in grid size shown in Table 5.1. Inspection of their  $\overline{w'\theta'}$  profiles confirms a relatively deeper scaled region of negative flux as compared with those seen here (.4 vs .25). Their surface heat flux  $\overline{w'\theta'}_s$  was twice the highest used here, but their range of  $Ri$  is comparable to that of this study. The latter point although not directly relevant here, serves as confirmation that  $\gamma$  is the more influential parameter.

**Table 5.3:** EZ Definitions used in comparable Studies

Publication	EZ Depth	CBL height	$\theta$ Jump
Federovich et al. (2004)	$z_{f1} - z_{f0}$	$z_f$	$\bar{\theta}(z_{f1}) - \bar{\theta}(z_{f0})$
Brooks and Fowler (2012)	$2 \times (z_f - z_{f0})$	$z_f$	average of local values

### 5.3.2 General Comparison using the Potential Temperature Profile

Here, when heights are defined based on the scaled vertical potential temperature gradient profile  $\frac{\partial \bar{\theta}}{\partial z}$  the curve representing Equation 1.15

$$\frac{\Delta h}{h} \propto Ri^b \quad (1.15)$$

shows an exponent  $b$  which increases in magnitude, from about  $-\frac{1}{2}$  as predicted and seen by Boers (1989), to about  $-1$  as justified in Nelson et al. (1989), with increasing  $Ri$  (decreasing  $Ri^{-1}$ ). Overall there is a clear narrowing of the scaled EZ depth with increasing  $Ri$  (decreasing  $Ri^{-1}$ ) as supported by the local height distributions in Section 4.1.1. Although based on different height definitions, Federovich et al. (2004) concluded an exponent  $b = -\frac{1}{2}$  and Brooks and Fowler's (2012) plots show curves with an apparent exponent less in magnitude than  $-1$ , in Figure 5.3.

The curves representing each run in Figure 5.3 fan out. In Figure 4.12 of this thesis, before scaling, the  $\frac{\partial \bar{\theta}}{\partial z}$  profile curves separate out, but in the reverse order. CBLs under higher stability, and so higher  $Ri$ , have larger scaled EZ depths. Whereas Brooks and Fowler's (2012) runs with initially lower  $Ri$  have larger scaled EZ depths than those with higher, even where  $Ri$  values overlap. Nonetheless, that there appears a family of separate but similar

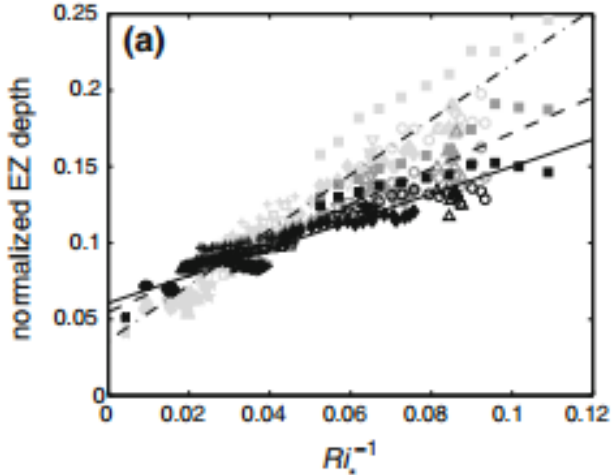


**Figure 5.3:** Panel (a) from Figure 5 in Brooks and Fowler (2012) representing Equation 1.15: The normalized EZ depth is determined in three ways (i) the upper and lower percentiles from the distribution of local CBL height (maximum tracer gradient), normalized by the average of the local heights (pale grey) (ii) the average of local scaled EZ depths based on wavelet covariance (dark grey) and (iii) the average of the locally determined EZ depths scaled by the average of the locally determined heights (black), based on wavelet covariance. Their  $\theta$  jump is an average of the potential temperature differences across the local EZ depths.

curves rather than a single curve hints at an underlying scaling parameter.

Neither study referenced in Table 3.3 addresses the change in exponent with increased  $Ri$  that I observe in Figure 4.17. It is reasonable to suggest that this represents a change in entrainment mechanism. Sullivan et al. (1998) observed enfolding and engulfment at lower  $Ri$ . Whereas at higher  $Ri$  when motion is more restricted, entrainment seemed to occur via trapping of thinner wisps at the edge of an upward moving thermal. Turner (1986) also distinguishes between entrainment by convective overturning and recoil. Garcia and Mellado (2014) refer to a change in entrainment rate due to the effects

of increased stability on the upper EZ sub-layer. In this study, the narrowing of the EZ depends predominantly on the magnitude of the average vertical potential temperature gradient  $\frac{\partial \bar{\theta}}{\partial z}$  in the lower EZ and upper ML. However, the scaled magnitude of upper limit in Figure ?? (a) does appear to decrease slightly in time. This could correspond to the slowly decreasing upper sub layer of the EZ mentioned in both Garcia and Mellado (2014) and Federovich et al. (2004).

## 5.4 Entrainment Rate Parameterization

$Ri$  magnitude determined in this and the comparable studies is primarily influenced by the magnitude of the  $\theta$  jump. Here, I define it in two ways as Federovich et al. (2004) did. I do this based on the  $\overline{w'\theta'}$  profile, as in Figure 4.20 and Table 4.1 for the purpose of direct comparison and to observe how the change in definition effects Equation 1.24.

$$\frac{w_e}{w^*} \propto Ri^a \quad (1.24)$$

### 5.4.1 Direct Comparison based on the vertical Heat Flux Profile

The larger jump, i.e. that taken across the EZ ( $\Delta\theta$ ) as in Figure 1.3, yields a larger value of  $a$  as Federovich et al. (2004) conclude. Garcia and Mellado (2014) interpret both curves as asymptotic to straight lines ( $a = -1$ ) as the upper EZ sub-layer narrows. Based on their plots in Figure 5.4, in the absence of their justification based on the derivation of the entrainment relation, for  $\Delta\theta$  I see a curve (grey and blue) with increasing exponent exceeding magnitude  $-1$  at higher  $Ri$ . For their version of  $\delta\theta$  I see a curve (grey and red) with exponent less in magnitude than  $-1$ .

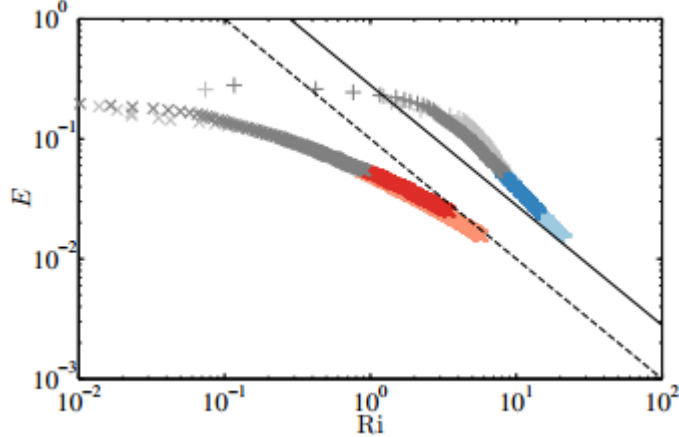


**Figure 5.4:** Figure 11 from Garcia and Mellado (2014) and representing equation 1.24 based on the two  $\theta$  jumps. The grey and blue curve is based on  $\Delta\theta$  and the (grey and) red curve is based on  $\bar{\theta}(h) - \bar{\theta}_0(h)$  which is slightly different to the  $\delta\theta$  defined here and in Federovich et al. (2004). The dashed and continuous black lines represent the straight lines to which the curves asymptote according to their analysis. Their heights are comparable to those based on the heat flux ( $w'\theta'$ ) profile in Figure 4.20.

#### 5.4.2 Extending Comparison to the average Potential Temperature Profile

There is an analogous distinction between curves representing Equation 1.24 using  $\Delta\theta$  and those using  $\delta\theta$ , when all heights are based on the  $\frac{\partial\bar{\theta}}{\partial z}$  profile. Scatter is least when the  $\theta$  jump is defined across the EZ. In Figure 4.25  $a = -\frac{3}{2}$  fits at higher  $Ri$  (lower  $Ri^{-1}$ ) and  $a = -1$  seems to fit at lower  $Ri$ . Combined with the apparent change in  $b$  for Equation 1.15 I interpret this as an indication of a change in entrainment regime at increasing  $Ri$ .

## 6. Conclusion

### 6.1 Major Findings

The dry idealized convective atmospheric boundary layer (CBL) was modeled using large eddy simulation (LES). Although this has been done before and a broad understanding of the dynamics and scaling behaviour has been established, discussion of details continues. This study was intended to contribute to this discussion and shed light on some of these details. It was guided by the questions outlined in Section 1.3 and answered in Chapter 5 and concludes with the following four points:

#### 6.1.1 The gradient Method for determining local Heights based on the $\theta$ Profile is problematic.

Local  $\theta$  profiles varies depending on location. The top of an active thermal impinging on the free atmosphere (FA) as in Figure 4.1 is characterized by a steep gradient comparable to the zero-order model representation in Figure 1.4. At other locations, for example where a thermal has overturned or recoiled and some entrainment has been initiated as in Figure 4.2, there is a region over which the  $\theta$  profile transitions to the upper lapse rate ( $\gamma$ ). That is, there is a local entrainment zone (EZ). At such locations, there are gradients well into the FA that exceed any within the EZ, as well as an absence of a definitive local CBL height. This presents both a practical and conceptual challenge to the gradient method, while determination of the ML using linear regression is more reliable.

### 6.1.2 CBL Height and EZ Boundaries can be defined based on the average Potential Temperature Profile

The  $\bar{\theta}$  profile characterizes the dry, idealized CBL and links bulk models to soundings via an LES. Both the EZ depth and CBL height based on the average  $\frac{\partial \bar{\theta}}{\partial z}$  profile showed dependence on  $Ri$  (Sections 4.2 and 4.3) as seen in other studies and justified theoretically. So this is a valid way of defining the CBL and its EZ.

### 6.1.3 Upper Lapse-Rate is a critical Parameter in idealized CBL Entrainment

The magnitude and variance of local height, increase with increasing  $\overline{w'\theta'_s}$ , and decrease with increasing  $\gamma$ . The same can be said for the vertical velocity fluctuations ( $w'$ ) in the EZ. However, increased  $\gamma$  results in an increase in the positive potential temperature fluctuations ( $\theta'^+$ ) at  $h$ . The magnitude of ( $\theta'^+$ ) at points where  $w'$  is negative represents downward moving entrained air and depends on  $\gamma$  (Section 4.1). Below  $h$ , in the lower EZ, the average vertical potential temperature gradient ( $\frac{\partial \bar{\theta}}{\partial z}$ ) also depends  $\gamma$  (Section 4.2.2). So, the growth of the idealized dry CBL is driven by  $\overline{w'\theta'_s}$  and suppressed by stability ( $\gamma$ ). But CBL warming is due, in part, to the entrainment of air from aloft the potential temperature of which in turn depends on  $\gamma$ .

Throughout this entire study, threads the influence of this parameter. Distributions of scaled local ML heights approach similarity, when  $\gamma$  is constant but  $\overline{w'\theta'_s}$  is varied (Figure 4.3). Curves representing Equation 1.15 group according to  $\gamma$  when based on the  $\frac{\partial \bar{\theta}}{\partial z}$  profile, but become similar once based on  $\frac{\partial \bar{\theta}}{\partial z}$  (Section 4.2.2). The convective time scale  $\tau = \frac{w^*}{h}$  and  $Ri$  group according  $\gamma$  (Figure 3.1) lending support to Federovich et al. (2004)'s use of a the Brunt-Vaisala time scale. It seems that once the effect of the surface heat flux ( $\overline{w'\theta'_s}$ ) is accounted for through  $h$ ,  $\gamma$  emerges as the dominant parameter in dry, idealized CBL entrainment.

#### **6.1.4 There are two CBL Entrainment Regimes**

Turner (1986) outlined and theoretically justified two distinct convective boundary layer entrainment regimes wherein the scaled entrainment rates have different  $Ri$  dependence. The LES flow visualizations of Sullivan et al. (1998) showed large scale engulfment at lower  $Ri$ . At higher  $Ri$ , trapping of smaller volumes of stable air between and at the edges of impinging thermals appeared to be the dominant mechanism. The CBL entrainment zone measurements analyzed in Traumner et al. (2011) further support the concept of varying entrainment mechanism depending on the strength of the upper lapse rate  $\gamma$ . Finally, both Federovich et al. (2004) and Garcia and Mellado (2014) discuss the varying dependence of the scaled entrainment rate on  $Ri$  as the effects of upper stability become more important. On these grounds I attribute the change in exponent in the plots of equations 1.15 and 1.24 in Figures 4.17 and 4.25 to a change in entrainment regime as  $Ri$  increases.

## **6.2 Future Work**

Some ideas as to how the work in this thesis could be completed or extended is as follows:

### **6.2.1 Expand local CBL height determination Method**

To further the tri-linear regression method described in Section 2.2.1, the EZ could be approximated by a 3rd order polynomial, fit using an appropriate regression method. It then could be possible to determine a local CBL height at the point of maximum gradient on this fitted curve.

### **6.2.2 Examine Resolution Effects**

Runs could be carried out at lower resolution, to examine the effects on the curves in Figure 4.19 and eliminate or confirm this as a cause for disagreement with the results of Federovich et al. (2004). The height and  $\theta$  jump definitions of Garcia and Mellado (2014) could be matched to facilitate di-

rect comparison with their results and speak more to the need for increased resolution.

### 6.2.3 Further explore Entrainment Regimes

As discussed, there is sufficient cause to assume there is a change in entrainment mechanism as  $Ri$  increases. Animated visualizations of two-dimensional horizontal slices showed thermals regularly impinging on the FA with associated, intermittent periods of vigorous activity. A possible way to observe these mixing events and how they change with respect to  $Ri$  and time, is to measure velocity and vorticity at local points, or sub-domain regions. The connection between increased horizontal and downward motions in the EZ, and CBL growth can, easily be tested by concurrently measuring the local height. Furthermore, activity measured at different levels within the EZ could shed further light on the turbulence characteristics of Garcia and Mellado's (2014) suggested two layer structure.

### 6.2.4 Apply a Mass Flux Scheme

The robustness of equations 1.15 and 1.24 could be tested by first establishing criteria for determining the CBL locally and then calculating the entrainment rate based on the increase in volume of this layer using the method described in Dawe and Austin (2010). CBL air could be identified using a passive tracer, and or potential temperature. The EZ could, for example, be defined based on statistics of local CBL heights.

## References

- Batchvarova, E. and S.-E. Gryning, 1994: An applied model for the height of the daytime mixed layer and the entrainment zone. *Boundary-Layer Meteorology*, **71**, 311–323.
- Betts, A. K., 1974: Reply to comment on the paper: "non-precipitating cumulous convection and its parametrization". *Quart. J. Roy. Meteor. Soc.*, **100**, 469 – 471.
- Boers, R., 1989: A parametrization of the depth of the entrainment zone. *Journal of Applied Meteorology*, 107–111.
- Brooks, I. M. and A. M. Fowler, 2012: An evaluation of boundary-layer depth, inversion and entrainment parameters by large-eddy simulation. *Boundary-Layer Meteorology*, **142**, 245–263.
- Crum, T. D. and R. B. Stull, 1987: Field measurements of the amount of surface layer air versus height in the entrainment zone. *Journal of the Atmospheric Sciences*, **44**, 2743 – 2753.
- Crum, T. D., R. B. Stull, and E. W. Eloranta, 1987: Coincident lidar and aircraft observations of entrainment into thermals and mixed layers. *Journal of Climate and Applied Meteorology*, **26**, 774–788.
- Dawe, J. T. and P. H. Austin, 2010: Interpolation of les cloud surfaces for use in direct calculations of entrainment and detrainment. *Monthly Weather Review*, **139**, 444–456.
- Deardorff, J. W., 1970: Convective velocity and temperature scales for the unstable planetary boundary layer and for rayleigh convection. *Journal of the Atmospheric Sciences*, **27**, 1211 – 1213.
- Deardorff, J. W., 1972: Numerical investigation of neutral and unstable planetary boundary layers. *Journal of the Atmospheric Sciences*, **29**, 91 – 115.

- Deardorff, J. W., 1979: Prediction of convective mixed-layer entrainment for realistic capping inversion structure. *Journal of the Atmospheric Sciences*, **36**, 424–436.
- Deardorff, J. W., G. E. Willis, and B. J. Stockton, 1980: Laboratory studies of the entrainment zone of a convectively mixed layer. *J. Fluid Mech.*, **100**, 41–64.
- Ebert, E. E., U. Schumann, and R. B. Stull, 1989: Nonlocal turbulent mixing in the convective boundary layer evaluated from large-eddy simulation. *Journal of the Atmospheric Sciences*, **46**, 2178 – 2207.
- Federovich, E., R. Conzemus, and D. Mironov, 2004: Convective entrainment into a shear-free, linearly stratified atmosphere: Bulk models reevaluated through large eddy simulation. *Journal of the Atmospheric Sciences*, **61**, 281 – 295.
- Fedorovich, E. and R. Conzemius, 2001: *Large Eddy Simulation of Convective Entrainment in Linearly and Discretely Stratified Fluids*. 1st ed., Kluwer Academic Publishers.
- Garcia, J. R. and J. P. Mellado, 2014: The two-layer structure of the entrainment zone in the convective boundary layer. *Journal of the Atmospheric Sciences*, doi:10.1175/JAS-D-130148.1.
- Khairoutdinov, M. F. and D. A. Randall, 2003: Cloud resolving model of the arm summer 1997 iop: Model formulation results, uncertainties and sensitivities. *Journal of the Atmospheric Sciences*, **60**, 607–623.
- Kolmogorov, A. N., 1962: A refinement of previous hypotheses concerning the local structure of turbulence in a viscous incompressible fluid at high Reynolds number. *Journal of Fluid Mechanics*, **13**, 82–85.
- Mahrt, L. and J. Paumier, 1984: Heat transport in the atmospheric boundary layer. *Journal of the Atmospheric Sciences*, **41**, 3061–3075.
- Nelson, E., R. Stull, and E. Eloranta, 1989: A prognostic relationship for entrainment zone thickness. *Journal of Applied Meteorology*, **28**, 885–901.
- Schmidt, H. and U. Schumann, 1989: Coherent structure of the convective boundary layer derived from large-eddy simulations. *J. Fluid Mech.*, **200**, 511–562.

- Sorbjan, Z., 1996: Effects caused by varying the strength of the capping inversion based on a large eddy simulation model of the shear-free convective boundary layer. *Journal of the Atmospheric Sciences*, **53**, 2015–2024.
- Steyn, D. G., M. Baldi, and R. M. Hoff, 1999: The detection of mixed layer depth and entrainment zone thickness from lidar backscatter profiles. *Journal of Atmospheric and Oceanic Technology*, **16**, 953–959.
- Stull, R., 1973: Inversion rise model based on penetrative convection. *Journal of the Atmospheric Sciences*, **30**, 1092–1099.
- Stull, R., 1988: *An Introduction to Boundary Layer Meteorology*. 1st ed., Kluwer Academic Publishers.
- Stull, R. B., 1976a: The energetics of entrainment across a density interface. *Journal of the Atmospheric Sciences*, **33**, 1260 – 1267.
- Stull, R. B., 1976b: Mixed layer depth model based on turbulent energetics. *Journal of the Atmospheric Sciences*, **33**, 1268 – 1278.
- Sullivan, P. P., C.-H. Moeng, B. Stevens, D. H. Lenschow, and S. D. Mayor, 1998: Structure of the entrainment zone capping the convective atmospheric boundary layer. *Journal of the Atmospheric Sciences*, **55**, 3042–3063, doi:10.1007/s10546-011-9668-3.
- Sullivan, P. P. and E. G. Patton, 2011: The effect of mesh resolution on convective boundary layer statistics and structures generated by large eddy simulation. *Journal of the Atmospheric Sciences*, **58**, 2395–2415, doi:10.1175/JAS-D-10-05010.1.
- Tennekes, H., 1973: A model for the dynamics of the inversion above a convective boundary layer. *Journal of the Atmospheric Sciences*, **30**, 558–566.
- Traumner, K., C. Kottmeier, U. Corsmeier, and A. Wieser, 2011: Convective boundary-layer entrainment: Short review and progress using doppler lidar. *Boundary-Layer Meteorology*, **141**, 369–391, doi:10.1007/s10546-011-9657-6.
- Turner, J. S., 1986: Turbulent entrainment: the development of the entrainment assumption and its application to geophysical flows. *J. Fluid Mech.*, **173**, 431–471.

- Vieth, E., 2011: Fitting piecewise linear regression functions to biological responses. *Journal of Applied Physiology*, **67**, 390–396.
- Wilde, N. P., R. A. Stull, and E. W. Eloranta, 1985: The lcl zone and cumulous onset. *Journal of Climate and Applied Meteorology*, **24**, 640 – 657.

## 7. Appendices

### 7.1 Potential Temperature: $\theta$

$$\theta = T \left( \frac{p_0}{p} \right)^{\frac{R_d}{c_p}} \quad (7.1)$$

$p_0$  and  $p$  are a reference pressure and pressure respectively.

$$\frac{c_p}{\theta} \frac{d\theta}{dt} = \frac{c_p}{T} \frac{dT}{dt} - \frac{R_d}{p} \frac{dp}{dt} \quad (7.2)$$

If changes in pressure are negligible compared to overall pressure, as in the case of that part atmosphere that extends from the surface to 2km above it.

$$c_p \frac{d\theta}{\theta} = c_p \frac{dT}{T} - \frac{R_d}{p} \frac{dp}{dt} \quad (7.3)$$

$$\frac{d\theta}{\theta} = \frac{dT}{T} \quad (7.4)$$

and if

$$\frac{\theta}{T} \approx 1 \quad (7.5)$$

then small changes in temperature are approximated by small changes in potential temperature

$$d\theta \approx dT \text{ or } \theta' \approx T' \quad (7.6)$$

and at constant pressure change in enthalpy ( $H$ ) is

$$dH = c_p dT. \quad (7.7)$$

This serves as justification for defining  $\overline{w' \theta'}$  as the vertical heat flux.

## 7.2 Second Law of Thermodynamics

$$\frac{ds}{dt} \geq \frac{q}{T} \quad (7.8)$$

For a reversible process

$$\frac{ds}{dt} = \frac{q}{T} \quad (7.9)$$

Using the first law and the equation of state for an ideal gas

$$\frac{q}{T} = \frac{1}{T} \left( \frac{dh}{dt} - \alpha \frac{dp}{dt} \right) = \frac{c_p}{T} \frac{dT}{dt} - \frac{R_d}{p} \frac{dp}{dt} \quad (7.10)$$

so

$$\frac{ds}{dt} = \frac{q}{T} = \frac{c_p}{\theta} \frac{d\theta}{dt} \quad (7.11)$$

For a dry adiabatic atmosphere

$$\frac{ds}{dt} = \frac{c_p}{\theta} \frac{d\theta}{dt} = 0 \quad (7.12)$$

## 7.3 Reynolds Decomposition and Simplification of Conservation of Enthalpy (or Entropy) for a dry Atmosphere

$$\frac{\partial \theta}{\partial t} + u_i \frac{\partial \theta}{\partial x_i} = \nu_\theta \frac{\partial^2 \theta}{\partial x_i^2} - \frac{1}{c_p} \frac{\partial Q^*}{\partial x_i} \quad (7.13)$$

$\nu$  and  $Q^*$  are the thermal diffusivity and net radiation respectively. If we ignore these two effects then

$$\frac{\partial \theta}{\partial t} + u_i \frac{\partial \theta}{\partial x_i} = 0 \quad (7.14)$$

$$\theta = \bar{\theta} + \theta', \theta = \bar{u}_i + u'_i \quad (7.15)$$

$$\frac{\partial \bar{\theta}}{\partial t} + \frac{\partial \theta'}{\partial t} + \bar{u}_i \frac{\partial \bar{\theta}}{\partial x_i} + u'_i \frac{\partial \bar{\theta}}{\partial x_i} + \bar{u}_i \frac{\partial \theta'}{\partial x_i} + u'_i \frac{\partial \theta'}{\partial x_i} = 0 \quad (7.16)$$

Averaging and getting rid of average variances and their linear products

$$\frac{\partial \bar{\theta}}{\partial t} + \bar{u}_i \frac{\partial \bar{\theta}}{\partial x_i} + u'_i \frac{\partial \bar{\theta}'}{\partial x_i} = 0 \quad (7.17)$$

Ignoring mean winds

$$\frac{\partial \bar{\theta}}{\partial t} + u'_i \frac{\partial \bar{\theta}'}{\partial x_i} = 0 \quad (7.18)$$

using flux form

$$\frac{\partial \bar{\theta}}{\partial t} + \frac{\partial (\bar{u}'_i \bar{\theta}')}{\partial x_i} - \theta' \frac{\partial \bar{u}'_i}{\partial x_i} = 0 \quad (7.19)$$

under the bousinesq assumption  $\Delta \cdot u_i = 0$

$$\frac{\partial \bar{\theta}}{\partial t} = - \frac{\partial (\bar{u}'_i \bar{\theta}')}{\partial z} \quad (7.20)$$

ignoring horizontal fluxes

$$\frac{\partial \bar{\theta}}{\partial t} = - \frac{\partial (\bar{w}' \bar{\theta}')}{\partial z} \quad (7.21)$$

## 7.4 Reynolds averaged Turbulence Kinetic Energy Equation

$$\frac{\partial \bar{e}}{\partial t} + \bar{U}_j \frac{\partial \bar{e}}{\partial x_j} = \delta_{i3} \frac{g}{\bar{\theta}} (\bar{u}'_i \bar{\theta}') - \bar{u}'_i \bar{u}'_j \frac{\partial \bar{U}_i}{\partial x_j} - \frac{\partial (\bar{u}'_j e')}{\partial x_j} - \frac{1}{\bar{\rho}} \frac{\partial (\bar{u}'_i p')}{\partial x_i} - \epsilon \quad (7.22)$$

$e$  is turbulence kinetic energy (TKE).  $p$  is pressure.  $\rho$  is density.  $\epsilon$  is viscous dissipation.